# Smooth optimization algorithms for global and locally low-rank regularizers

Rodrigo A. Lobos[†*], Javier Salazar-Cavazos[†], Raj Rao Nadakuditi[†], and Jeffrey A. Fessler[†]

**Abstract.**
Many inverse problems and signal processing problems involve low-rank regularizers based on the nuclear norm. Commonly, proximal gradient methods (PGM) are adopted to solve this type of non-smooth problems as they can offer fast and guaranteed convergence. However, PGM methods cannot be simply applied in settings where low-rank models are imposed locally on overlapping patches; therefore, heuristic approaches have been proposed that lack convergence guarantees. In this work we propose to replace the nuclear norm with a smooth approximation in which a Huber-type function is applied to each singular value. By providing a theoretical framework based on singular value function theory, we show that important properties can be established for the proposed regularizer, such as: convexity, differentiability, and Lipschitz continuity of the gradient. Moreover, we provide a closed-form expression for the regularizer gradient, enabling the use of standard iterative gradient-based optimization algorithms (e.g., nonlinear conjugate gradient) that can easily address the case of overlapping patches and have well-known convergence guarantees. In addition, we provide a novel step-size selection strategy based on a quadratic majorizer of the line-search function that leverages the Huber characteristics of the proposed regularizer. Finally, we assess the proposed optimization framework by providing empirical results in dynamic magnetic resonance imaging (MRI) reconstruction in the context of locally low-rank models with overlapping patches.

## 1. Introduction.

Some inverse problems and many signal processing problems involving low-rank models are formulated as optimization problems using global low-rank regularizers as follows[1]:

$$\hat{\boldsymbol{X}} = \underset{\boldsymbol{X} \in \mathbb{C}^{M \times N}}{\arg\min}\; f(\boldsymbol{X}) + \beta \left\| \boldsymbol{X} \right\|_* , \tag{1.1}$$

where $\|\cdot\|_*$ denotes the nuclear norm. Example applications include robust PCA [5], matrix completion [11, 18], parallel MRI [28, 71, 72], low-rank + sparse models for dynamic MRI [51], among many others [10, 12, 23, 27, 64, 66, 69].

In the usual case where $f$ has a Lipschitz continuous gradient, these optimization problems are solved easily using proximal gradient methods like the proximal optimized gradient method (POGM) [31, 60], as the nuclear norm is non-smooth but "prox friendly." Empirical results in dynamic MRI show that POGM converges faster than FISTA for such cost functions [42]. Nevertheless, these first-order (accelerated) proximal gradient methods have worst-case $O(1/k^2)$ convergence rates that can be slow compared to optimization methods for

[*]Department of Biomedical Engineering, University of Michigan, Ann Arbor, MI, 48109 (rlobos@umich.edu)
[†]Department of Electrical Engineering and Computer Science, University of Michigan, Ann Arbor, MI, 48109 (javiersc@umich.edu, rajnrao@umich.edu, fessler@umich.edu)

**Funding:** Research supported in part by NIH Grants R01 EB023618, U01 EB026977, R01 EB035618, R21 EB034344, and R21 AG061839, NSF grant 2331590.

[1]Throughout the paper we use capital and lower case bold letters to denote matrices and vectors, respectively. The entry in the $k$th row and $l$th column of a matrix $\boldsymbol{X}$ is denoted either as $X_{kl}$ or $[\boldsymbol{X}]_{kl}$. Analogously, the $k$th entry of a vector $\boldsymbol{x}$ is denoted either as $x_k$ or $[\boldsymbol{x}]_k$. Besides the nuclear norm, in later derivations we also use the Frobenius norm for matrices, denoted by $\|\cdot\|_{\mathrm{F}}$. For vectors, we denote by $\|\cdot\|$ and $\|\cdot\|_\infty$ the $\ell_2$-norm and the $\ell_\infty$-norm, respectively.

smooth problems [17,54]. Augmented Lagrangian and ADMM algorithms are another option, but these require additional tuning parameters and do not have faster convergence rates. Additional limitations for proximal gradient methods are encountered when using locally low-rank models, where low-rank characteristics are promoted locally on overlapping patches constructed from $\boldsymbol{X}$. Applications include: matrix approximation [33], MRI reconstruction [56, 63], dynamic MRI [16, 30, 62], multi-contrast and quantitative MRI [59, 67], MR denoising [46], fMRI denoising [15, 47, 65], fMRI dynamic image reconstruction [20], and MR motion correction [9]. As an example, in dynamic MRI reconstruction the optimization problem has the form[2]:

$$\hat{\boldsymbol{X}} = \underset{\boldsymbol{X} \in \mathbb{C}^{M \times N}}{\arg\min}\ f(\boldsymbol{X}) + \beta \sum_{\boldsymbol{s} \in \Lambda} \sum_{\boldsymbol{p} \in \Gamma} \left\| \mathcal{P}_{\boldsymbol{p}}(\mathcal{S}_{\boldsymbol{s}}(\boldsymbol{X})) \right\|_*, \tag{1.2}$$

where $\Lambda, \Gamma \subseteq \mathbb{Z}^d$ are sets of shift and location indexes, respectively, and $d$ corresponds to the image voxel dimensions[3]; $\mathcal{S}_{\boldsymbol{s}} : \mathbb{C}^{M \times N} \to \mathbb{C}^{M \times N}$ is a linear operator that circularly shifts the images composing the columns of $\boldsymbol{X}$ according to the shift index $\boldsymbol{s}$; and $\mathcal{P}_{\boldsymbol{p}} : \mathbb{C}^{M \times N} \to \mathbb{C}^{P \times N}$ is a linear operator that constructs a matrix from a patch extracted from $\boldsymbol{X}$ whose entries depend on the location index $\boldsymbol{p}$. In many applications these patches are considered overlapping (*i.e.*, share entries of $\boldsymbol{X}$), which makes standard proximal algorithms unsuitable for solving (1.2), as there is no known simple proximal mapping for the regularizer in this case. This challenge has led to various heuristics like "cycle spinning" [61], proximal averaging [1], and other approaches that do not have any convergence guarantees [70]. Replacing the nuclear norm with a *smooth approximation* could facilitate the use of standard iterative gradient-based optimization algorithms like nonlinear conjugate gradients (NCG), or perhaps even second-order optimization methods like quasi-Newton methods. These algorithms might lead to faster convergence while providing convergence guarantees. Moreover, they could be applied directly to the locally low-rank formulation even in the case of overlapping patches.

The nuclear norm in (1.1) is a convex relaxation of a regularizer based on the rank of $\boldsymbol{X}$, so it is already a kind of approximation to the "ideal" low-rank model. Thus, it seems quite reasonable to entertain further approximations. This work investigates the use of smooth regularizers instead of non-smooth alternatives such as the nuclear norm. Specifically, we study regularizers of the form:

$$R_\psi(\boldsymbol{X}) \triangleq \sum_{k=1}^{r} \psi(\sigma_k(\boldsymbol{X})), \tag{1.3}$$

where $r = \min(M, N)$; $\sigma_k(\boldsymbol{X})$ denotes the $k$th singular value of $\boldsymbol{X}$ and $\psi$ is a smooth function subject to mild regularity conditions. We study the case where $\psi$ satisfies the so-called Huber conditions [26, p. 184], which is why we call $R_\psi$ a *Huber-based low-rank regularizer*. Then, we propose to impose global low-rank models by solving:

$$\hat{\boldsymbol{X}} = \underset{\boldsymbol{X} \in \mathbb{C}^{M \times N}}{\arg\min}\ \Psi_{\text{Global}}(\boldsymbol{X}), \quad \Psi_{\text{Global}}(\boldsymbol{X}) = f(\boldsymbol{X}) + \beta R_\psi(\boldsymbol{X}), \tag{1.4}$$

[2]Here we briefly describe the dynamic MRI reconstruction optimization problem using locally low-rank regularizers. Section 6 provides more details.

[3]For simplicity we consider $d = 2$ throughout the paper (*i.e.*, 2D images); however, our results can be easily extended to higher dimensions.

and to impose locally low-rank models by solving:

$$\hat{\boldsymbol{X}} = \underset{\boldsymbol{X}\in\mathbb{C}^{M\times N}}{\arg\min}\ \Psi_{\text{Local}}(\boldsymbol{X}), \quad \Psi_{\text{Local}}(\boldsymbol{X}) = f(\boldsymbol{X}) + \beta \sum_{\boldsymbol{s}\in\Lambda}\sum_{\boldsymbol{p}\in\Gamma} R_\psi(\mathcal{P}_{\boldsymbol{p}}(\mathcal{S}_{\boldsymbol{s}}(\boldsymbol{X}))). \tag{1.5}$$

The local case with overlapping patches is our primary motivation, since that is the case where the regularizer is not "prox friendly."

A representative example for $\psi$ is the hyperbola:

$$\psi(t) = \delta^2\sqrt{1+(t/\delta)^2}, \tag{1.6}$$

which is approximately $\delta\,|t|$ for $t \gg \delta > 0$, so it can approximate the nuclear norm very well by taking $\delta$ to be small (*cf.* Fig. 1.a). We will also explore choices of $\psi$ that are non-convex (but still smooth) (*cf.* Fig. 1.d). Non-convex Schatten-$p$ quasi-norms with $0 < p < 1$ have also been investigated as beneficial alternatives to the nuclear norm, *e.g.*, [50]. Other non-convex functions of the singular values have also been investigated, *e.g.*, [6, 8, 22, 49].

The regularizer proposed in (1.3) corresponds to a unitarily invariant function [34], and therefore it only depends on the singular values. Functions with these characteristics are known as singular value functions [39, 40], and their properties (*e.g.*, convexity, differentiability, Lipschitz continuity of the gradient) have been extensively investigated over the last two decades [34, 36–40, 53, 57, 58]. However, to the best of our knowledge, the application of these properties has not been explored in inverse problems using low-rank models. In this work we show that relevant properties for the optimization of $R_\psi$ are directly related to the analogous properties of $\psi$. Using these derivations, we show that it is possible to use standard gradient-based iterative optimization algorithms (*e.g.*, NCG, quasi-Newton methods) to solve (1.4) and (1.5).

Iterative gradient-based optimization algorithms usually require two main computations: the cost function gradient, and a step size in each iteration that guarantees a decrease of the cost function. We show that the gradient of the cost function can be calculated in closed form by relying on singular value function theory to calculate $\nabla R_\psi(\boldsymbol{X})$. Then we provide a step-size selection strategy that exploits the Huber/Lipschitz characteristics of $\psi$. Given two arbitrary (fixed) matrices $\boldsymbol{X}, \boldsymbol{\Delta} \in \mathbb{C}^{M\times N}$, we show that the 1D line search function $h : \mathbb{R} \to \mathbb{R}$ defined as[4]:

$$h(\alpha; \boldsymbol{X}, \boldsymbol{\Delta}) \triangleq \Psi(\boldsymbol{X} + \alpha\boldsymbol{\Delta}), \tag{1.7}$$

where $\Psi$ can be either $\Psi_{\text{Global}}$ or $\Psi_{\text{Local}}$, can be monotonically decreased using a majorize-minimize approach. Specifically, we propose a dynamic step-size selection strategy where a quadratic majorizer is constructed for $h$ at each iteration by leveraging on the Huber conditions satisfied by $\psi$. This construction is based on deriving novel majorizers for the proposed regularizer $R_\psi$, which is one of our main theoretical contributions in this work.

In addition, we generalize our theoretical framework by considering a weighted version of the proposed regularizers, that we call *weighted Huber-based low-rank regularizers*. Specifically,

[4]Throughout the paper we use the notation $f(\cdot\ ;\ \cdot)$ to indicate that the function $f$ depends on parameters that are given after the semicolon symbol ; .

we study regularizers of the form:

$$R_{\psi,\boldsymbol{w}}(\boldsymbol{X}) \triangleq \sum_{k=1}^{r} w_k \, \psi(\sigma_k(\boldsymbol{X})), \tag{1.8}$$

where $\boldsymbol{w} = [w_1, \ldots, w_r]^T$ corresponds to a nonzero vector of nonnegative weights, and $(\cdot)^T$ denotes the transpose operation. To properly impose low-rank models, $R_{\psi,\boldsymbol{w}}$ should penalize more small singular values than large singular values, as the former are usually associated with noise in real applications. This property suggests that the weights should be nondecreasing, *i.e.*, $0 \leq w_1 \leq w_2 \leq \ldots \leq w_r$. However, we show that under this setting $R_{\psi,\boldsymbol{w}}$ is nonconvex, which is relevant from an optimization perspective. A similar analysis was provided by Chen et al. in [8] for the adaptive nuclear norm; we extend their results to the family of weighted Huber-based low-rank regularizers. Interestingly, if $\psi$ is selected as the hyperbola function, the regularizer in (1.8) can be interpreted as a smooth version of the adaptive nuclear norm [8]. One relevant case where the weights are nondecreasing is when the first $K$ entries of $\boldsymbol{w}$ are equal to zero and the remaining entries are equal to one. If $K$ is a good approximation of the true rank, then $R_{\psi,\boldsymbol{w}}$ would promote low-rank characteristics by penalizing only the tail singular values without affecting the first $K$ singular values. We call this version of the weighted regularizer a *tail Huber-based low-rank regularizer*. As an example, if $\psi$ is selected as the hyperbola function, this tail regularizer can be interpreted as a smooth version of the regularizer used in [6, 49] for robust PCA applications, which corresponds to the sum of the tail singular values. Analogously, if $\psi$ is selected as the parabola function, *i.e.*, $\psi(t) = t^2$, this tail regularizer matches the regularizer proposed in [22], which has been extensively used in MRI reconstruction applications [4, 24, 32, 45] and also used in computed tomography (CT) restoration [43]. Analogously to the analysis we provide for $R_\psi$, we study the convexity and differentiability of $R_{\psi,\boldsymbol{w}}$ and the Lipschitz continuity of its gradient. We show that the proposed optimization framework can be extended such that $R_{\psi,\boldsymbol{w}}$ can be used instead of $R_\psi$.

The explicit gradient calculation of the cost function, jointly with the step-size selection strategy provided in this work, can be seen as the main steps of a smooth optimization framework for inverse problems using low-rank models. Remarkably, by enabling standard gradient-based iterative optimization algorithms, it is possible to solve (1.5) in the case of overlapping patches while also providing convergence guarantees. Moreover, the same optimization algorithm can be used for different choices of $\psi$ when Huber's conditions are satisfied. This offers users a convenient mechanism to explore different regularizers; however, this flexibility might decrease computational speed compared to algorithms that are designed for a particular non-smooth regularizer. We show in the context of dynamic MRI reconstruction that our proposed framework can converge faster and provide better image quality than state-of-the-art algorithms (*e.g.*, POGM) that are tailored to commonly used non-smooth regularizers.

This paper is organized as follows. Section 2 provides a detailed description of the proposed Huber-based low-rank regularizers; their convexity and differentiability properties are studied by establishing connections with singular value functions. Section 3 introduces novel majorizers for the proposed regularizers that are used to show the Lipschitz continuity of the regularizer gradient, and to provide a quadratic majorizer for the line search function in later sections. Section 4 extends the proposed theoretical framework to weighted Huber-based

low-rank regularizers. Section 5 provides a smooth optimization framework based on the proposed Huber-based low-rank regularizers to minimize (1.4) or (1.5) using standard iterative gradient-based optimization algorithms. Section 6 illustrates the applicability of the proposed optimization framework in the context of dynamic MRI reconstruction using locally low-rank models with overlapping patches. Finally, Section 7 provides discussion and conclusions.

## 2. Huber-based low-rank regularizers.

Let $\boldsymbol{X} \in \mathbb{C}^{M\times N}$ be a rectangular matrix with singular values $\sigma_1(\boldsymbol{X}) \geq \sigma_2(\boldsymbol{X}) \geq \ldots \geq \sigma_r(\boldsymbol{X}) \geq 0$ where $r = \min(M, N)$, and let the vector-valued function $\boldsymbol{\sigma} : \mathbb{C}^{M\times N} \to \mathbb{R}^r$ defined as $\boldsymbol{\sigma}(\boldsymbol{X}) \triangleq [\sigma_1(\boldsymbol{X}), \ldots, \sigma_r(\boldsymbol{X})]^T$. Using this notation, we write the proposed low-rank regularizer in (1.3) as:

$$R_\psi(\boldsymbol{X}) = (f_\psi \circ \boldsymbol{\sigma})(\boldsymbol{X}), \tag{2.1}$$

where $\circ$ denotes function composition; $f_\psi : \mathbb{R}^r \to \mathbb{R}$ is defined as $f_\psi(\boldsymbol{x}) \triangleq \sum_{k=1}^r \psi(x_k)$; and $\psi : \mathbb{R} \to \mathbb{R}$ corresponds to a function satisfying the Huber conditions [26, p. 184], which we refer as the *potential function*. The extra notation introduced to write the regularizer expression in (2.1) might seem redundant, but it facilitates the study of the properties of $R_\psi$ in later sections. In fact, the expression in (2.1) reveals that $R_\psi$ corresponds to a singular value function [34,39] that involves the potential function, as indicated later in this section. Notably, relevant properties for the optimization of the regularizer highly depend on the analogous properties of the potential function. For this reason we provide a detailed description of the latter in the following subsection.

### 2.1. Huber potential functions.

The potential function $\psi$ in (1.3) and (2.1) satisfies the following Huber conditions [26, p. 184]:

(i) $\psi$ is differentiable.

(ii) $\psi$ is even, *i.e.*, $\psi(t) = \psi(-t), \forall t \in \mathbb{R}$.

(iii) $\omega_\psi(t) \triangleq \dot{\psi}(t)/t$, where $\dot{\psi}$ denotes the derivative of $\psi$, is bounded, nonnegative and monotone nonincreasing for $t > 0$. This function is called the *weighting function*.

This family of functions, collectively called Huber potential functions, is extensive, and includes convex and non-convex functions that have been widely used in inverse problems, e.g., [7, 19]. The assumption that $\omega_\psi$ is nonnegative means that $\dot{\psi}$ must be nonnegative for $t > 0$, which means that $\psi$ must be nondecreasing for $t > 0$. There are examples of redescending potential functions in the imaging literature [14, 68] (although perhaps not in terms of singular values). We leave extensions to descending $\psi$ for future work.

A notable property of a potential function $\psi$ is that it always has a quadratic majorizer having curvature $\omega_\psi$. Specifically, for any $s \in \mathbb{R}$, the function

$$q_\psi(t; s) \triangleq \psi(s) + \dot{\psi}(s)(t - s) + \frac{1}{2}\,\omega_\psi(s)(t - s)^2 \tag{2.2}$$

satisfies:

$$\psi(s) = q_\psi(s; s), \tag{2.3}$$

$$\psi(t) \leq q_\psi(t; s), \quad \forall t \in \mathbb{R}. \tag{2.4}$$

Moreover, $q_\psi$ is the quadratic majorizer for $\psi$ satisfying (2.3) and (2.4) with optimal (i.e., smallest) curvature [26, p. 186]. This surrogate will be particularly useful when studying

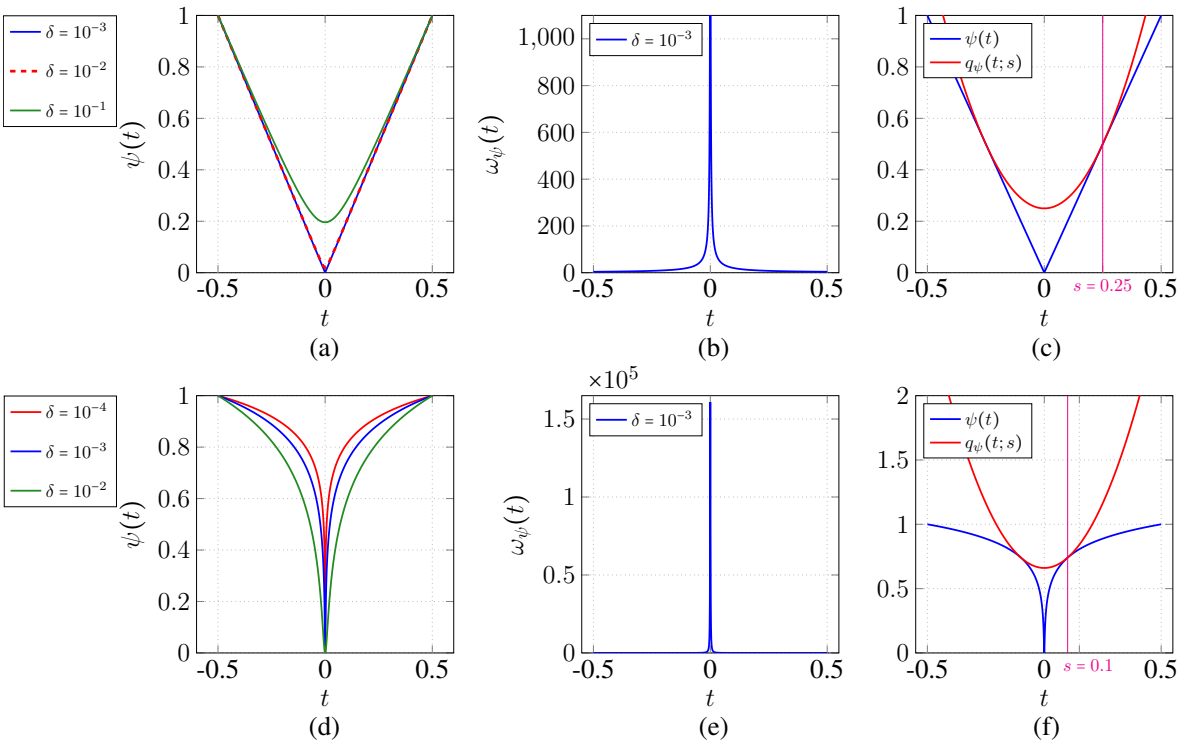


Figure 1: Examples of Huber potential functions. (a) Hyperbola function (convex) as defined in (1.6) for three values of $\delta$. Each curve has been normalized for illustration purposes. The respective potential weighting function is shown in (b) for $\delta = 10^{-3}$. For this case (c) shows the quadratic majorizer as defined in (2.2) for a particular value of $s$. (d,e,f) show analogous results for the Cauchy function (non-convex) as defined in (2.6).

majorizers for $R_\psi$ in Section 3. Interestingly, this surrogate also allows one to show that $\dot{\psi}$ is Lipschitz continuous. Given that $\omega_\psi$ is symmetric and monotonically nonincreasing for $t > 0$, it follows that:

$$\begin{aligned} \psi(t) \leq q_\psi(t;s) &\leq \psi(s) + \dot{\psi}(s)(t-s) + \frac{1}{2}\left(\sup_{t\in\mathbb{R}} \omega_\psi(t)\right)(t-s)^2, \quad \forall t, s \in \mathbb{R}, \\ &= \psi(s) + \dot{\psi}(s)(t-s) + \frac{1}{2}\,\omega_\psi(0)(t-s)^2, \end{aligned} \tag{2.5}$$

which is equivalent to $\dot{\psi}$ being $\omega_\psi(0)$-Lipschitz [2, Thm. 5.8].

Figure 1 shows two examples of potential functions with their respective weighting functions and quadratic majorizers. Figure 1.a illustrates the (convex) hyperbola function already introduced in (1.6), and Fig. 1.b illustrates the (non-convex) Cauchy potential function

$$\psi(t) = \frac{1}{2}\delta^2 \log\left(1 + \left(\frac{t}{\delta}\right)^2\right). \tag{2.6}$$

The following subsection shows that many of the properties of the potential function $\psi$ (*e.g.*, convexity, differentiability, Lipschitz continuity of the derivative) are transferred to the regularizer $R_\psi$ as a direct consequence of $R_\psi$ being a singular value function. For this purpose, in the following derivations we consider $\mathbb{C}^{M\times N}$ as a vector space endowed with the (Frobenius) inner product $\langle \cdot\ ,\ \cdot \rangle : \mathbb{C}^{M\times N} \times \mathbb{C}^{M\times N} \to \mathbb{C}$ defined as:

$$\langle \boldsymbol{A},\, \boldsymbol{B} \rangle = \mathsf{trace}\big\{\boldsymbol{A}\boldsymbol{B}'\big\},\ \forall \boldsymbol{A}, \boldsymbol{B} \in \mathbb{C}^{M\times N}, \tag{2.7}$$

where $(\cdot)'$ denotes the Hermitian transpose operation.

**2.2. Properties of Huber-based low-rank regularizers.** The regularizer proposed in (1.3) and (2.1) is contained in a class of functions known as unitarily invariant functions or *singular value functions* [34,36,37,39,40], which in general terms are functions that depend only on the singular values of the matrix argument. For completeness, we provide the formal definition in the following.

Definition 2.1 (Unitarily invariant function or singular value function [34, 39, 40]). *A function $F : \mathbb{C}^{M\times N} \to [-\infty, +\infty]$ is unitarily invariant if $F(\boldsymbol{U}\boldsymbol{X}\boldsymbol{V}) = F(\boldsymbol{X})$ for any $\boldsymbol{X} \in \mathbb{C}^{M\times N}$ and any suitably sized unitary matrices $\boldsymbol{U}$ and $\boldsymbol{V}$. $F(\boldsymbol{X})$ is also called a singular value function as it depends only on the singular values of $\boldsymbol{X}$.*

To facilitate the analysis of the proposed regularizers we also need the following definition.

Definition 2.2 (Absolutely symmetric function [34]). *A function $f : \mathbb{R}^r \to [-\infty, +\infty]$ is absolutely symmetric if $f(\boldsymbol{x}) = f(\check{\boldsymbol{x}})$ for any vector $\boldsymbol{x} \in \mathbb{R}^r$, where $\check{\boldsymbol{x}} \in \mathbb{R}^r$ corresponds to the vector formed by arranging the entries of the vector $|\boldsymbol{x}| \triangleq [|x_1|, \ldots, |x_r|]^T$ in nonincreasing order.*

There is a one-to-one correspondence between unitarily invariant functions defined on $\mathbb{C}^{M\times N}$ and absolutely symmetric functions defined on $\mathbb{R}^r$ [34]. In fact, if $f : \mathbb{R}^r \to [-\infty, +\infty]$ is absolutely symmetric, then $f \circ \boldsymbol{\sigma}$ is unitarily invariant. Conversely, if $F : \mathbb{C}^{M\times N} \to [-\infty, +\infty]$ is unitarily invariant, then $f(\boldsymbol{x}) = F(\mathsf{Diag}\{\boldsymbol{x}\})$ is absolutely symmetric, where $\mathsf{Diag} : \mathbb{R}^r \to \mathbb{C}^{M\times N}$ corresponds to a linear operator that creates a rectangular diagonal matrix using the entries of its input. Specifically, the entry in the $k$th row and $l$th column of $\mathsf{Diag}\{\boldsymbol{x}\} \in \mathbb{C}^{M\times N}$ is given by $[\mathsf{Diag}\{\boldsymbol{x}\}]_{kl} = x_k$ if $k = l$ and 0 otherwise. Establishing the correspondence between singular value functions and absolutely symmetric functions is important, as many relevant properties of $F$ are directly related to the analogous properties of the corresponding absolutely symmetric function $f$. Particularly, convexity and differentiability were studied by Lewis and Sendov in [34, 36, 39, 40]. We summarize these results in the following proposition as these properties are relevant to our optimization framework.

Proposition 2.3 (Convexity and differentiability of singular value functions [34,36,39,40]). *Let $F = f \circ \boldsymbol{\sigma} : \mathbb{C}^{M\times N} \to [-\infty, +\infty]$ be a singular value function with corresponding absolutely symmetric function $f : \mathbb{R}^r \to [-\infty, +\infty]$. Then,*

*(i) $F$ is convex if and only if $f$ is convex.*

*(ii) If $f$ is convex, then $F$ is differentiable at $\boldsymbol{X} \in \mathbb{C}^{M\times N}$ if and only if $f$ is differentiable at $\boldsymbol{\sigma}(\boldsymbol{X})$. In this case the gradient of $F$ is given by:*

$$\nabla F(\boldsymbol{X}) = \boldsymbol{U}\, \mathsf{Diag}\{\nabla f(\boldsymbol{\sigma}(\boldsymbol{X}))\}\, \boldsymbol{V}', \tag{2.8}$$

*where* $\boldsymbol{U}$ *and* $\boldsymbol{V}$ *are suitably sized unitary matrices such that* $\boldsymbol{X} = \boldsymbol{U}\,\mathsf{Diag}\{\boldsymbol{\sigma}(\boldsymbol{X})\}\,\boldsymbol{V}'$.

*(iii) If* $f$ *is non-convex and locally Lipschitz around* $\boldsymbol{\sigma}(\boldsymbol{X})$*, then* $F$ *is differentiable at* $\boldsymbol{X}$ *if and only if* $f$ *is differentiable at* $\boldsymbol{\sigma}(\boldsymbol{X})$*. The gradient of* $F$ *is given by (2.8).*

We can study the nuclear norm as an example of the previous theorem. The nuclear norm is clearly unitarily invariant, and its corresponding absolutely symmetric function is given by $f_*(\boldsymbol{x}) \triangleq \sum_{k=1}^{r} |x_k|$, *i.e.*, $\|\boldsymbol{X}\|_* = (f_* \circ \boldsymbol{\sigma})(\boldsymbol{X})$. The function $f_*$ also corresponds to a symmetric gauge function [48]. It can be shown that absolutely symmetric functions correspond to symmetric gauge functions when, in addition, they are positively homogeneous [35]. Given that $f_*$ is convex and non-differentiable at points where some of the entries are equal to zero, then, according to Theorem 2.3, $\|\cdot\|_*$ is convex and non-differentiable at matrices where some of the singular values are equal to zero.

In our setting, it is straightforward to show that the function $f_\psi$ in (2.1) is absolutely symmetric and therefore the corresponding regularizer $R_\psi$ is a singular value function (*i.e.*, unitarily invariant). Then, we can establish conditions for the convexity and differentiability of $R_\psi$ by analyzing $f_\psi$ and using Proposition 2.3. In our context, these conditions are directly related to the potential function $\psi$ as stated in the next theorem. Appendix A gives the straightforward proof.

Theorem 2.4 (Convexity and differentiability of Huber-based low-rank regularizers). *Let* $R_\psi$ *be a Huber-based low-rank regularizer defined as in (1.3) and (2.1). Then,*

*(i)* $R_\psi$ *is convex if and only if* $\psi$ *is convex.*

*(ii)* $R_\psi$ *is differentiable at* $\boldsymbol{X} \in \mathbb{C}^{M\times N}$ *and its gradient is given by:*

$$\nabla R_\psi(\boldsymbol{X}) = \boldsymbol{U}\,\mathsf{Diag}\Big\{\dot{\psi}.(\boldsymbol{\sigma}(\boldsymbol{X}))\Big\}\,\boldsymbol{V}', \tag{2.9}$$

*where* $\boldsymbol{U}$ *and* $\boldsymbol{V}$ *are suitably sized unitary matrices such that* $\boldsymbol{X} = \boldsymbol{U}\,\mathsf{Diag}\{\boldsymbol{\sigma}(\boldsymbol{X})\}\,\boldsymbol{V}'$.

In (2.9), $\dot{\psi}.(\boldsymbol{\sigma}(\boldsymbol{X}))$ denotes the vector formed by applying the function $\dot{\psi}$ element-wise to the vector $\boldsymbol{\sigma}(\boldsymbol{X})$, *i.e.*, $\dot{\psi}.(\boldsymbol{\sigma}(\boldsymbol{X})) = [\dot{\psi}(\sigma_1(\boldsymbol{X})), \ldots, \dot{\psi}(\sigma_r(\boldsymbol{X}))]^T$. This notation arises in the Julia language [3] and we use it throughout.

Remark 2.5. *The differentiability of* $R_\psi$ *is independent of its convexity, so we do not have two cases as Proposition 2.3 might suggest. This is because* $f_\psi$ *is always locally Lipschitz as* $\nabla f_\psi$ *is Lipschitz continuous, which happens even when* $\psi$ *is non-convex. This follows from the fact that* $\dot{\psi}$ *is Lipschitz continuous (*cf.*, (2.5)). Appendix A provides more details in the proof of Theorem 2.4.*

Another important property to study is the Lipschitz continuity of $\nabla R_\psi(\boldsymbol{X})$. Specifically, we want to determine conditions under which $\nabla R_\psi$ is Lipschitz continuous. By following the same principles in Theorem 2.4, the next proposition shows that these conditions are directly related to the Lipschitz properties of $\dot{\psi}$. Appendix C gives a proof for this proposition based on the results in Section 3.

Proposition 2.6 (Lipschitz continuity of the gradient of Huber-based low-rank regularizers). *Let* $R_\psi$ *be a regularizer defined as in (1.3) and (2.1). Then,* $\nabla R_\psi$ *is* $L$*-Lipschitz continuous where* $L = \omega_\psi(0)$*, i.e.,*

$$\|\nabla R_\psi(\boldsymbol{X}) - \nabla R_\psi(\boldsymbol{Y})\|_{\mathrm{F}} \leq \omega_\psi(0)\,\|\boldsymbol{X} - \boldsymbol{Y}\|_{\mathrm{F}}\,,\ \forall \boldsymbol{X}, \boldsymbol{Y} \in \mathbb{C}^{M\times N}. \tag{2.10}$$

The properties shown in Theorem 2.4 and Proposition 2.6 suffice to enable standard iterative gradient-based optimization methods for solving (1.4) and (1.5) as shown in Section 5; however, the fast convergence of these optimization methods highly depends on the adopted step-size selection rule. The next section proposes a new class of majorizers for Huber-based low-rank regularizers. These majorizers are then used to propose efficient step-size selection strategies that enable the fast convergence of iterative gradient-based optimization methods when using Huber-based low-rank regularizers.

**3. Majorizers for Huber-based low-rank regularizers.** The previous section showed that many relevant properties of the potential function $\psi$ are transferred to the Huber-based low-rank regularizer $R_\psi$. Following this principle, and given that quadratic majorizers can be defined for $\psi$ as shown in (2.2), this section derives novel majorizers for $R_\psi$. Inspired by the work of Lewis and Sendov in [38], that derives a quadratic expansion to approximate spectral functions defined on real symmetric matrices, here we provide a general expression for majorizers for Huber-based low-rank regularizers. Our results are directly stated in the more general case where Huber-based low-rank regularizers are defined on complex rectangular matrices.

A majorizer for $R_\psi$ at $\boldsymbol{S} \in \mathbb{C}^{M\times N}$, denoted by $Q(\cdot\,;\boldsymbol{S})$, should satisfy:

$$R_\psi(\boldsymbol{S}) = Q(\boldsymbol{S};\boldsymbol{S}), \tag{3.1}$$

$$R_\psi(\boldsymbol{X}) \leq Q(\boldsymbol{X};\boldsymbol{S}), \quad \forall \boldsymbol{X} \in \mathbb{C}^{M\times N}. \tag{3.2}$$

We show below that (3.1) and (3.2) are satisfied for functions with the form:

$$Q(\boldsymbol{X};\boldsymbol{S},G_\psi) = R_\psi(\boldsymbol{S}) + \mathrm{real}\{\langle \nabla R_\psi(\boldsymbol{S}),\, \boldsymbol{X}-\boldsymbol{S}\rangle\} + \frac{1}{2}(\mathbf{1}'_M(G_\psi(\boldsymbol{\sigma}(\boldsymbol{S}))\odot|\boldsymbol{U}'(\boldsymbol{X}-\boldsymbol{S})\boldsymbol{V}|.\hat{}2)\mathbf{1}_N), \tag{3.3}$$

where $\mathbf{1}_K$ denotes a vector of length $K$ with each entry equal to one; $\odot$ denotes entry-wise (Hadamard) product; $\boldsymbol{U}$ and $\boldsymbol{V}$ are suitably sized unitary matrices such that $\boldsymbol{S} = \boldsymbol{U}\,\mathsf{Diag}\{\boldsymbol{\sigma}(\boldsymbol{S})\}\,\boldsymbol{V}'$; and $G_\psi : \mathbb{R}^r \to \mathbb{C}^{M\times N}$ is an operator that depends on $\psi$ that constructs a matrix out of the entries of its input. Finally, the notation $|\boldsymbol{A}|.\hat{}2$ for $\boldsymbol{A} \in \mathbb{C}^{M\times N}$ corresponds to a matrix in $\mathbb{R}^{M\times N}$ whose entries are the entries of $\boldsymbol{A}$ after taking the absolute value and square operations entry-wise. If $\boldsymbol{B} = |\boldsymbol{A}|.\hat{}2$, then $B_{kl} = |A_{kl}|^2$. In the following we show that two specific operators, denoted by $G^{\mathrm{R}}_\psi$ and $G^{\mathrm{L}}_\psi$, make the corresponding function defined in (3.3) a majorizer for $R_\psi$. If $\boldsymbol{s} \in \mathbb{R}^r$ and $M < N$ (wide case), $G^{\mathrm{R}}_\psi$ is defined as:

$$G^{\mathrm{R}}_\psi(\boldsymbol{s}) \triangleq (\omega_\psi.(\boldsymbol{s}))\,\mathbf{1}'_N, \tag{3.4}$$

and when $M > N$ (tall case):

$$G^{\mathrm{R}}_\psi(\boldsymbol{s}) \triangleq \mathbf{1}_M\,(\omega_\psi.(\boldsymbol{s}))'. \tag{3.5}$$

For both the wide and tall cases the second operator is defined as:

$$G^{\mathrm{L}}_\psi(\boldsymbol{s}) \triangleq \omega_\psi(0)\,\mathbf{1}_M\mathbf{1}'_N. \tag{3.6}$$

The following theorem states that $Q(\cdot\,;\boldsymbol{S},G^{\mathrm{R}}_\psi)$ and $Q(\cdot\,;\boldsymbol{S},G^{\mathrm{L}}_\psi)$ are majorizers for $R_\psi$ at $\boldsymbol{S} \in \mathbb{C}^{M\times N}$, and it also provides equivalent expressions for both functions. Appendix B provides its proof.

Theorem 3.1 (Majorizers for Huber-based low-rank regularizers). *Let $\boldsymbol{S} \in \mathbb{C}^{M\times N}$ and $\boldsymbol{U}, \boldsymbol{V}$ suitably sized unitary matrices such that $\boldsymbol{S} = \boldsymbol{U}\,\mathsf{Diag}\{\boldsymbol{\sigma}(\boldsymbol{S})\}\,\boldsymbol{V}'$. Then $Q(\cdot\,;\boldsymbol{S}, G_\psi^{\mathrm{R}})$ and $Q(\cdot\,;\boldsymbol{S}, G_\psi^{\mathrm{L}})$ are both majorizers for $R_\psi$ at $\boldsymbol{S} \in \mathbb{C}^{M\times N}$, i.e., both satisfy (3.1) and (3.2). If $M < N$ (wide case), then*

$$Q(\boldsymbol{X};\boldsymbol{S}, G_\psi^{\mathrm{R}}) = R_\psi(\boldsymbol{S}) + \mathrm{real}\{\langle \nabla R_\psi(\boldsymbol{S}),\, \boldsymbol{X}-\boldsymbol{S}\rangle\} + \frac{1}{2}\left\|\boldsymbol{W}'_{\psi,\boldsymbol{S}}\,(\boldsymbol{X}-\boldsymbol{S})\right\|_{\mathrm{F}}^2, \tag{3.7}$$

*where the matrix $\boldsymbol{W}_{\psi,\boldsymbol{S}}$ is defined as*

$$\boldsymbol{W}_{\psi,\boldsymbol{S}} \triangleq \boldsymbol{U}\,\mathsf{Diag}\left\{\sqrt{\omega_\psi.(\boldsymbol{\sigma}(\boldsymbol{s}))}\right\}\boldsymbol{V} \in \mathbb{C}^{M\times N}, \tag{3.8}$$

*where the square-root is applied element-wise. If $M > N$ (tall case), then*

$$Q(\boldsymbol{X};\boldsymbol{S}, G_\psi^{\mathrm{R}}) = R_\psi(\boldsymbol{S}) + \mathrm{real}\{\langle \nabla R_\psi(\boldsymbol{S}),\, \boldsymbol{X}-\boldsymbol{S}\rangle\} + \frac{1}{2}\left\|(\boldsymbol{X}-\boldsymbol{S})\,\boldsymbol{T}'_{\psi,\boldsymbol{S}}\right\|_{\mathrm{F}}^2, \tag{3.9}$$

*where the matrix $\boldsymbol{T}_{\psi,\boldsymbol{S}}$ is defined as:*

$$\boldsymbol{T}_{\psi,\boldsymbol{S}} \triangleq \boldsymbol{U}'\,\mathsf{Diag}\left\{\sqrt{\omega_\psi.(\boldsymbol{\sigma}(\boldsymbol{s}))}\right\}\boldsymbol{V}' \in \mathbb{C}^{M\times N}. \tag{3.10}$$

*For the wide and tall cases we have that:*

$$Q(\boldsymbol{X};\boldsymbol{S}, G_\psi^{\mathrm{L}}) = R_\psi(\boldsymbol{S}) + \mathrm{real}\{\langle \nabla R_\psi(\boldsymbol{S}),\, \boldsymbol{X}-\boldsymbol{S}\rangle\} + \frac{1}{2}\,\omega_\psi(0)\,\|\boldsymbol{X}-\boldsymbol{S}\|_{\mathrm{F}}^2. \tag{3.11}$$

The following subsection uses Theorem 3.1 to derive quadratic majorizers for the 1D line search function associated with the proposed regularizer. The construction of these quadratic majorizers is one of our main results because it provides a simple step-size selection strategy that ensures monotonic descent in the optimization framework proposed in Section 5.

### 3.1. Quadratic majorizers for the line search function of Huber-based low-rank regularizers.

Using Theorem 3.1, we show in the following that quadratic majorizers can be constructed for the regularizer 1D line search function $h_\psi : \mathbb{R} \to \mathbb{R}$ defined as:

$$h_\psi(\alpha;\boldsymbol{X},\boldsymbol{\Delta}) \triangleq R_\psi(\boldsymbol{X}+\alpha\boldsymbol{\Delta}), \tag{3.12}$$

where $\alpha \in \mathbb{R}$ and $\boldsymbol{X}, \boldsymbol{\Delta} \in \mathbb{C}^{M\times N}$ are two arbitrary (fixed) matrices. The following theorem provides a general form for these quadratic majorizers. Appendix D provides its proof using Theorem 3.1.

Theorem 3.2. *Let $G_\psi : \mathbb{R}^r \to \mathbb{C}^{M\times N}$ be an operator such that $Q(\cdot\,;\boldsymbol{X}+\bar{\alpha}\boldsymbol{\Delta}, G_\psi)$, defined as in (3.3), is a majorizer for $R_\psi$ at $\boldsymbol{X}+\bar{\alpha}\boldsymbol{\Delta}$ where $\bar{\alpha} \in \mathbb{R}$. Define the quadratic function*

$$g_{h_\psi}(\alpha;\bar{\alpha},\boldsymbol{X},\boldsymbol{\Delta},G_\psi) \triangleq c_{h_\psi}^{(0)}(\bar{\alpha},\boldsymbol{X},\boldsymbol{\Delta}) + c_{h_\psi}^{(1)}(\bar{\alpha},\boldsymbol{X},\boldsymbol{\Delta})(\alpha-\bar{\alpha}) + \frac{1}{2}c_{h_\psi}^{(2)}(\bar{\alpha},\boldsymbol{X},\boldsymbol{\Delta},G_\psi)(\alpha-\bar{\alpha})^2 \tag{3.13}$$

*with coefficients given by:*

$$c^{(0)}_{h_\psi}(\bar{\alpha}, \boldsymbol{X}, \boldsymbol{\Delta}) = R_\psi(\boldsymbol{X} + \bar{\alpha}\boldsymbol{\Delta}) = h_\psi(\bar{\alpha}; \boldsymbol{X}, \boldsymbol{\Delta}), \tag{3.14}$$

$$c^{(1)}_{h_\psi}(\bar{\alpha}, \boldsymbol{X}, \boldsymbol{\Delta}) = \mathrm{real}\{\langle \nabla R_\psi(\boldsymbol{X} + \bar{\alpha}\boldsymbol{\Delta}),\, \boldsymbol{\Delta}\rangle\}, \tag{3.15}$$

$$c^{(2)}_{h_\psi}(\bar{\alpha}, \boldsymbol{X}, \boldsymbol{\Delta}, G_\psi) = \mathbf{1}'_M(G_\psi(\boldsymbol{\sigma}(\boldsymbol{X} + \bar{\alpha}\boldsymbol{\Delta})) \odot |\boldsymbol{U}'\boldsymbol{\Delta}\boldsymbol{V}|.\hat{}2)\mathbf{1}_N, \tag{3.16}$$

*where $\boldsymbol{U}, \boldsymbol{V}$ are suitable sized unitary matrices such that $\boldsymbol{X} + \bar{\alpha}\boldsymbol{\Delta} = \boldsymbol{U}\,\mathsf{Diag}\{\boldsymbol{\sigma}(\boldsymbol{X} + \bar{\alpha}\boldsymbol{\Delta})\}\,\boldsymbol{V}'$. Then, $g_{h_\psi}(\alpha; \bar{\alpha}, \boldsymbol{X}, \boldsymbol{\Delta}, G_\psi)$ is a quadratic majorizer for $h_\psi(\alpha; \boldsymbol{X}, \boldsymbol{\Delta})$ at $\bar{\alpha}$.*

Combining the results of Theorem 3.1 and Theorem 3.2 yields the following corollary that can guide the construction of quadratic majorizers for $h_\psi$ in practice.

Corollary 3.3. *$g_{h_\psi}(\alpha; \bar{\alpha}, \boldsymbol{X}, \boldsymbol{\Delta}, G^{\mathrm{R}}_\psi)$ and $g_{h_\psi}(\alpha; \bar{\alpha}, \boldsymbol{X}, \boldsymbol{\Delta}, G^{\mathrm{L}}_\psi)$ are both quadratic majorizers for $h_\psi(\alpha; \boldsymbol{X}, \boldsymbol{\Delta})$ at $\bar{\alpha}$, and*

$$g_{h_\psi}(\alpha\ ; \bar{\alpha}, \boldsymbol{X}, \boldsymbol{\Delta}, G^{\mathrm{R}}_\psi) \leq g_{h_\psi}(\alpha\ ; \bar{\alpha}, \boldsymbol{X}, \boldsymbol{\Delta}, G^{\mathrm{L}}_\psi),\ \forall \alpha \in \mathbb{R}.$$

Appendix E provides the proof of this corollary.

Before showing how to use the previous results in the proposed optimization framework in Section 5, the following section shows that all these previous results extend to the proposed weighted Huber-based low-rank regularizers defined in (1.8).

**4. Weighted Huber-based low-rank regularizers.** The regularizer $R_{\psi,\boldsymbol{w}}$ defined in (1.8) is unitarily invariant because it can be written as:

$$R_{\psi,\boldsymbol{w}}(\boldsymbol{X}) = (f_{\psi,\boldsymbol{w}} \circ \boldsymbol{\sigma})(\boldsymbol{X}), \tag{4.1}$$

where $f_{\psi,\boldsymbol{w}} : \mathbb{R}^r \to \mathbb{R}$ is defined as the absolutely symmetric function

$$f_{\psi,\boldsymbol{w}}(\boldsymbol{x}) \triangleq \sum\nolimits_{k=1}^{r} w_k\, \psi([\check{\boldsymbol{x}}]_k)\,. \tag{4.2}$$

Then, according to Proposition 2.3, we can assess the convexity and differentiability of $R_{\psi,\boldsymbol{w}}$ by studying $f_{\psi,\boldsymbol{w}}$. To simplify the following analysis, we assume that $\psi$ is not a constant and that $\boldsymbol{w}$ is nonzero. Both of these assumptions are reasonable in practice, as a constant potential function or having all weights equal to zero would not properly promote low-rank characteristics when constructing $R_{\psi,\boldsymbol{w}}$. Under these assumptions we begin studying the convexity of $f_{\psi,\boldsymbol{w}}$, which depends on the weights $\boldsymbol{w}$ and the potential function $\psi$ as shown in the following proposition.

Proposition 4.1. *$f_{\psi,\boldsymbol{w}}$ is convex if and only if the Huber potential $\psi$ is convex and $w_1 \geq w_2 \geq \ldots \geq w_r \geq 0$.*

Appendix F provides the proof. The following proposition provides conditions for the differentiability of $f_{\psi,\boldsymbol{w}}$ at vectors that are relevant in our analysis. Interestingly, these conditions do not depend on the vector $\boldsymbol{w}$.

Proposition 4.2. *Let $\boldsymbol{x} \in \mathbb{R}^r$ be a vector whose entries are unique, nonnegative, and arranged in decreasing order,* i.e., *$\boldsymbol{x} = \check{\boldsymbol{x}}$ and $x_k > x_{k+1},\ \forall k \in \{1 \ldots, r-1\}$. Then, $f_{\psi,\boldsymbol{w}}$ is locally Lipschitz and differentiable at $\boldsymbol{x}$ with gradient given by:*

$$\nabla f_{\psi,\boldsymbol{w}}(\boldsymbol{x}) = \boldsymbol{w} \odot \dot{\psi}.(\boldsymbol{x}). \tag{4.3}$$

Appendix G provides the proof.

The previous results allow us to establish conditions for the convexity and differentiability of $R_{\psi,\boldsymbol{w}}$. We summarize these results in the following theorem, which is provided without proof as it is a direct application of Proposition 2.3 using Proposition 4.1 and Proposition 4.2.

Theorem 4.3 (Convexity and differentiability of weighted Huber-based low-rank regularizers). *(i) $R_{\psi,\boldsymbol{w}}$ is convex if and only if $\psi$ is convex and $w_1 \geq w_2 \geq \ldots \geq w_r \geq 0$.*

*(ii) If $\boldsymbol{X} \in \mathbb{C}^{M\times N}$ has no repeated singular values,* i.e., *$\sigma_1(\boldsymbol{X}) > \sigma_2(\boldsymbol{X}) > \ldots > \sigma_r(\boldsymbol{X}) \geq 0$, then $R_{\psi,\boldsymbol{w}}$ is differentiable at $\boldsymbol{X}$ and*

$$\nabla R_{\psi,\boldsymbol{w}}(\boldsymbol{X}) = \boldsymbol{U}\,\mathsf{Diag}\Big\{\boldsymbol{w}\odot\dot{\psi}.(\boldsymbol{\sigma}(\boldsymbol{X}))\Big\}\,\boldsymbol{V}', \tag{4.4}$$

*where $\boldsymbol{U}$ and $\boldsymbol{V}$ are suitably sized unitary matrices such that $\boldsymbol{X} = \boldsymbol{U}\,\mathsf{Diag}\{\boldsymbol{\sigma}(\boldsymbol{X})\}\,\boldsymbol{V}'$.*

Remark 4.4. *In applications we might like low-rank regularizers to penalize small singular values more than large singular values, as the former are usually associated with noise. This preference would suggest using weights $\boldsymbol{w}$ whose components are in nondecreasing order,* i.e., *$0 \leq w_1 \leq w_2 \leq \ldots \leq w_r$. Under this setting Theorem 4.3 shows that $R_{\psi,\boldsymbol{w}}$ would be non-convex, which can complicate optimization. We show empirically in the following sections that in this non-convex setting $R_{\psi,\boldsymbol{w}}$ can outperform its non-weighted version $R_\psi$ when a good initialization is provided.*

Remark 4.5. *Theorem 4.3 provides a closed-form expression for $\nabla R_{\psi,\boldsymbol{w}}(\boldsymbol{X})$ which can be computed using a singular value decomposition (SVD) of $\boldsymbol{X}$. The existence of this gradient is based on the assumption that $\boldsymbol{X}$ does not have repeated singular values, which might seem limiting. However, in practice SVD solvers most likely provide distinct singular values due to numerical precision errors. Therefore, from now on we assume that the sufficient conditions of Theorem 4.3 are satisfied when calculating the gradient of $R_{\psi,\boldsymbol{w}}$.*

Under the setting of nondecreasing weights it is also possible to construct majorizers for $R_{\psi,\boldsymbol{w}}$ that are analogous to the ones provided for $R_\psi$ in (3.3). If $\boldsymbol{w} \in \mathbb{R}^r$ such that $0 \leq w_1 \leq w_2 \leq \ldots \leq w_r$, then these majorizers have the form:

$$\begin{aligned} Q_{\boldsymbol{w}}(\boldsymbol{X};\boldsymbol{S},G_{\psi,\boldsymbol{w}}) &= R_{\psi,\boldsymbol{w}}(\boldsymbol{S}) + \mathrm{real}\{\langle\nabla R_{\psi,\boldsymbol{w}}(\boldsymbol{S}),\,\boldsymbol{X}-\boldsymbol{S}\rangle\} \\ &\quad + \frac{1}{2}(\mathbf{1}_M'(G_{\psi,\boldsymbol{w}}(\boldsymbol{\sigma}(\boldsymbol{S}))\odot|\boldsymbol{U}'(\boldsymbol{X}-\boldsymbol{S})\boldsymbol{V}|.\hat{}2)\mathbf{1}_N), \end{aligned} \tag{4.5}$$

where $\boldsymbol{U},\boldsymbol{V}$ are suitably sized unitary matrices such that $\boldsymbol{S} = \boldsymbol{U}\,\mathsf{Diag}\{\boldsymbol{\sigma}(\boldsymbol{S})\}\,\boldsymbol{V}'$ and $G_{\psi,\boldsymbol{w}} : \mathbb{R}^r \to \mathbb{C}^{M\times N}$ is an operator that depends on $\psi$ and $\boldsymbol{w}$. Appendix H shows that two operators denoted by $G^{\mathrm{R}}_{\psi,\boldsymbol{w}}$ and $G^{\mathrm{L}}_{\psi,\boldsymbol{w}}$ provide valid majorizers for $R_{\psi,\boldsymbol{w}}$. Specifically, we state an extended version of Theorem 3.1. Using this theorem we can show that the gradient of $R_{\psi,\boldsymbol{w}}$ is Lipschitz continuous.

Proposition 4.6 (Lipschitz continuity of the gradient of weighted Huber-based low-rank regularizers). *For nonnegative and nondecreasing $\boldsymbol{w} \in \mathbb{R}^r$, $\nabla R_{\psi,\boldsymbol{w}}$ is $L$-Lipschitz continuous where $L = \|\boldsymbol{w}\|_\infty\,\omega_\psi(0)$, i.e.:*

$$\|\nabla R_{\psi,\boldsymbol{w}}(\boldsymbol{X}) - \nabla R_{\psi,\boldsymbol{w}}(\boldsymbol{Y})\|_{\mathrm{F}} \leq \|\boldsymbol{w}\|_\infty\,\omega_\psi(0)\,\|\boldsymbol{X}-\boldsymbol{Y}\|_{\mathrm{F}},\ \forall\boldsymbol{X},\boldsymbol{Y}\in\mathbb{C}^{M\times N}. \tag{4.6}$$

Appendix I provides the proof.

Using the previous results it is also possible to construct quadratic majorizers for the 1D function $h_{\psi,\boldsymbol{w}}(\alpha; \boldsymbol{X}, \boldsymbol{\Delta}) \triangleq R_{\psi,\boldsymbol{w}}(\boldsymbol{X} + \alpha\boldsymbol{\Delta})$. The procedure is analogous to the one described in Theorem 3.2 and is not provided for the sake of space.

**4.1. Tail Huber-based low-rank regularizers.** One important case is when the vector of weights is defined such that the first $K$ entries are equal to zero and the rest are equal to one, *i.e.*:

$$[\boldsymbol{w}_K]_k \triangleq \begin{cases} 0 & \text{if } k \leq K, \\ 1 & \text{otherwise,} \end{cases} \tag{4.7}$$

where $K \in \{0, \dots, r-1\}$. If $K$ is a good estimate of the true rank of $\boldsymbol{X}$, then $R_{\psi,\boldsymbol{w}_K}$ will not penalize the first $K$ singular values, as desired. It would only penalize the tail singular values. We call this version of the weighted regularizer the *tail Huber-based low-rank regularizer*:

$$R_{\psi,K}(\boldsymbol{X}) \triangleq R_{\psi,\boldsymbol{w}_K}(\boldsymbol{X}) = \sum_{k=K+1}^{r} \psi(\sigma_k(\boldsymbol{X})). \tag{4.8}$$

This regularizer is non-convex given that the entries of $\boldsymbol{w}_K$ are in nondecreasing order (see Theorem 4.3 part (i)). Nevertheless, we can calculate its gradient using Theorem 4.3 part (ii) and also construct majorizers for it using Theorem H.1. Therefore, it is possible to construct quadratic majorizers for the associated 1D line search function using the procedure in Theorem 3.2.

At this point we have derived a closed-form expression for the gradients of the proposed regularizers, and also provided quadratic majorizers for the associated 1D line search functions. Section 5 leverages these results to solve optimization problems (1.4) and (1.5) using standard iterative gradient-based optimization methods.

**5. Smooth optimization framework using Huber-based low-rank regularizers.** Instead of promoting low-rank models using the (non-smooth) nuclear norm in (1.1) and (1.2), we propose to use smooth Huber-based low-rank regularizers[5], *i.e.*, $R_\psi$ as defined in (1.3), to minimize (1.4) and (1.5).

Since (1.5) corresponds to a more general model than (1.4), we focus on the locally low-rank optimization problem. To use iterative gradient-based optimization algorithms to minimize $\Psi_{\text{Local}}$, we start by calculating its gradient by using Theorem 2.4. This gradient is simply given by:

$$\nabla \Psi_{\text{Local}}(\boldsymbol{X}) = \nabla f(\boldsymbol{X}) + \beta \sum_{\boldsymbol{s}\in\Lambda} \sum_{\boldsymbol{p}\in\Gamma} \mathcal{S}_{\boldsymbol{s}}^*(\mathcal{P}_{\boldsymbol{p}}^*(\nabla R_\psi(\mathcal{P}_{\boldsymbol{p}}(\mathcal{S}_{\boldsymbol{s}}(\boldsymbol{X}))))), \tag{5.1}$$

where $\nabla R_\psi(\mathcal{P}_{\boldsymbol{p}}(\mathcal{S}_{\boldsymbol{s}}(\boldsymbol{X})))$ is calculated using (2.9), and $\mathcal{S}_{\boldsymbol{s}}^*$ and $\mathcal{P}_{\boldsymbol{p}}^*$ correspond to the the adjoint operators of $\mathcal{S}_{\boldsymbol{s}}$ and $\mathcal{P}_{\boldsymbol{p}}$, respectively. This expression enables the minimization of $\Psi_{\text{Local}}$ using

[5]The following analysis can be easily extended to weighted Huber-based low-rank regularizers. We omit those derivations for the sake of notation simplicity.

gradient-based optimization algorithms like NCG or quasi-Newton methods; however, the fast convergence of these iterative algorithms highly depends on a step-size selection strategy that guarantees a monotonic decrease of $\Psi_{\text{Local}}$ in each iteration. The ideal step size can be determined by minimizing the line search function $h(\alpha\,;\boldsymbol{X},\boldsymbol{\Delta}) = \Psi_{\text{Local}}(\boldsymbol{X}+\alpha\boldsymbol{\Delta})$ where $\boldsymbol{X},\boldsymbol{\Delta} \in \mathbb{C}^{M\times N}$ are two arbitrary (fixed) matrices. For notation simplicity we define the matrices $\boldsymbol{X}^{(\boldsymbol{p},\boldsymbol{s})} \triangleq \mathcal{P}_{\boldsymbol{p}}(\mathcal{S}_{\boldsymbol{s}}(\boldsymbol{X}))$ and $\boldsymbol{\Delta}^{(\boldsymbol{p},\boldsymbol{s})} \triangleq \mathcal{P}_{\boldsymbol{p}}(\mathcal{S}_{\boldsymbol{s}}(\boldsymbol{\Delta}))$ where $(\boldsymbol{p},\boldsymbol{s}) \in \Gamma\times\Lambda$, and we also define the 1D functions

$$h_f(\alpha;\boldsymbol{X},\boldsymbol{\Delta}) \triangleq f(\boldsymbol{X}+\alpha\boldsymbol{\Delta}), \tag{5.2}$$

$$h_{\psi,\text{Local}}(\alpha;\boldsymbol{X},\boldsymbol{\Delta}) \triangleq \sum_{\boldsymbol{s}\in\Lambda}\sum_{\boldsymbol{p}\in\Gamma} h_\psi(\alpha;\boldsymbol{X}^{(\boldsymbol{p},\boldsymbol{s})},\boldsymbol{\Delta}^{(\boldsymbol{p},\boldsymbol{s})}), \tag{5.3}$$

where $h_\psi$ was defined in (3.12). Then, we can express the line search function $h$ as follows:

$$\begin{aligned} h(\alpha\,;\boldsymbol{X},\boldsymbol{\Delta}) &= \Psi_{\text{Local}}(\boldsymbol{X}+\alpha\boldsymbol{\Delta}) \\ &= f(\boldsymbol{X}+\alpha\boldsymbol{\Delta}) + \beta\sum_{\boldsymbol{s}\in\Lambda}\sum_{\boldsymbol{p}\in\Gamma} R_\psi(\mathcal{P}_{\boldsymbol{p}}(\mathcal{S}_{\boldsymbol{s}}(\boldsymbol{X}+\alpha\boldsymbol{\Delta}))) \\ &= f(\boldsymbol{X}+\alpha\boldsymbol{\Delta}) + \beta\sum_{\boldsymbol{s}\in\Lambda}\sum_{\boldsymbol{p}\in\Gamma} R_\psi(\mathcal{P}_{\boldsymbol{p}}(\mathcal{S}_{\boldsymbol{s}}(\boldsymbol{X})) + \alpha\mathcal{P}_{\boldsymbol{p}}(\mathcal{S}_{\boldsymbol{s}}(\boldsymbol{\Delta}))) \\ &= h_f(\alpha;\boldsymbol{X},\boldsymbol{\Delta}) + \beta\sum_{\boldsymbol{s}\in\Lambda}\sum_{\boldsymbol{p}\in\Gamma} h_\psi(\alpha;\boldsymbol{X}^{(\boldsymbol{p},\boldsymbol{s})},\boldsymbol{\Delta}^{(\boldsymbol{p},\boldsymbol{s})}) \\ &= h_f(\alpha;\boldsymbol{X},\boldsymbol{\Delta}) + \beta h_{\psi,\text{Local}}(\alpha;\boldsymbol{X},\boldsymbol{\Delta}), \end{aligned} \tag{5.4}$$

where the third equality follows from the linearity of $\mathcal{P}_{\boldsymbol{p}}$ and $\mathcal{S}_{\boldsymbol{s}}$. Thus, (5.4) reveals that $h(\alpha\,;\boldsymbol{X},\boldsymbol{\Delta})$ can be minimized by addressing the minimization of the functions $h_f(\alpha;\boldsymbol{X},\boldsymbol{\Delta})$ and $h_{\psi,\text{Local}}(\alpha;\boldsymbol{X},\boldsymbol{\Delta})$. Our strategy for this purpose is based on using quadratic majorizers for each of these 1D functions. In many inverse problems (*e.g.*, dynamic MRI reconstruction), $f$ has a quadratic structure and therefore it is straightforward to derive a quadratic majorizer for $h_f(\alpha;\boldsymbol{X},\boldsymbol{\Delta})$. Then, for the following derivations we assume that there exists a quadratic function defined as:

$$g_f(\alpha\,;\bar{\alpha},\boldsymbol{X},\boldsymbol{\Delta}) \triangleq c_f^{(0)}(\bar{\alpha},\boldsymbol{X},\boldsymbol{\Delta}) + c_f^{(1)}(\bar{\alpha},\boldsymbol{X},\boldsymbol{\Delta})(\alpha-\bar{\alpha}) + \frac{1}{2}c_f^{(2)}(\bar{\alpha},\boldsymbol{X},\boldsymbol{\Delta})(\alpha-\bar{\alpha})^2, \tag{5.5}$$

that is a majorizer for $h_f(\alpha;\boldsymbol{X},\boldsymbol{\Delta})$ at $\bar{\alpha}\in\mathbb{R}$, where $\{c_f^{(l)}(\bar{\alpha},\boldsymbol{X},\boldsymbol{\Delta})\}_{l=0}^2$ are three scalar coefficients that depend on $\bar{\alpha},\boldsymbol{X}$ and $\boldsymbol{\Delta}$. We use Theorem 3.2 and Corollary 3.3 to construct a quadratic majorizer for $h_{\psi,\text{Local}}(\alpha;\boldsymbol{X},\boldsymbol{\Delta})$. The following theorem provides this construction.

Theorem 5.1. *Let $G_\psi$ be an operator[6] such that $Q(\cdot\,;\boldsymbol{X}^{(\boldsymbol{p},\boldsymbol{s})}+\bar{\alpha}\boldsymbol{\Delta}^{(\boldsymbol{p},\boldsymbol{s})},G_\psi)$, defined as in (3.3), is a majorizer for $R_\psi$ at $\boldsymbol{X}^{(\boldsymbol{p},\boldsymbol{s})}+\bar{\alpha}\boldsymbol{\Delta}^{(\boldsymbol{p},\boldsymbol{s})}$, $\forall(\boldsymbol{p},\boldsymbol{s})\in\Gamma\times\Lambda$. Then, the quadratic function*

$$\begin{aligned} g_{h_{\psi,\text{Local}}}(\alpha\,;\bar{\alpha},\boldsymbol{X},\boldsymbol{\Delta},G_\psi) \triangleq\; & c^{(0)}_{h_{\psi,\text{Local}}}(\bar{\alpha},\boldsymbol{X},\boldsymbol{\Delta}) + c^{(1)}_{h_{\psi,\text{Local}}}(\bar{\alpha},\boldsymbol{X},\boldsymbol{\Delta})\,(\alpha-\bar{\alpha}) \\ & + \frac{1}{2}c^{(2)}_{h_{\psi,\text{Local}}}(\bar{\alpha},\boldsymbol{X},\boldsymbol{\Delta},G_\psi)\,(\alpha-\bar{\alpha})^2, \end{aligned} \tag{5.6}$$

[6]The input and output dimensions of $G_\psi$ are different in (3.13) and (5.6). We have adopted the same notation in both cases for simplicity, as the dimensions should be clear from context.

*with coefficients given by:*

$$c^{(0)}_{h_{\psi,\text{Local}}}(\bar{\alpha}, \boldsymbol{X}, \boldsymbol{\Delta}) = \sum_{\boldsymbol{s}\in\Lambda}\sum_{\boldsymbol{p}\in\Gamma} c^{(0)}_{h_\psi}(\bar{\alpha}, \boldsymbol{X}^{(\boldsymbol{p},\boldsymbol{s})}, \boldsymbol{\Delta}^{(\boldsymbol{p},\boldsymbol{s})}),$$

$$c^{(1)}_{h_{\psi,\text{Local}}}(\bar{\alpha}, \boldsymbol{X}, \boldsymbol{\Delta}) = \sum_{\boldsymbol{s}\in\Lambda}\sum_{\boldsymbol{p}\in\Gamma} c^{(1)}_{h_\psi}(\bar{\alpha}, \boldsymbol{X}^{(\boldsymbol{p},\boldsymbol{s})}, \boldsymbol{\Delta}^{(\boldsymbol{p},\boldsymbol{s})}), \tag{5.7}$$

$$c^{(2)}_{h_{\psi,\text{Local}}}(\bar{\alpha}, \boldsymbol{X}, \boldsymbol{\Delta}, G_\psi) = \sum_{\boldsymbol{s}\in\Lambda}\sum_{\boldsymbol{p}\in\Gamma} c^{(2)}_{h_\psi}(\bar{\alpha}, \boldsymbol{X}^{(\boldsymbol{p},\boldsymbol{s})}, \boldsymbol{\Delta}^{(\boldsymbol{p},\boldsymbol{s})}, G_\psi), \tag{5.8}$$

*is a majorizer for* $h_{\psi,\text{Local}}(\alpha\,;\boldsymbol{X},\boldsymbol{\Delta})$ *at* $\bar{\alpha}$.

*Proof.* It follows directly from using (3.13) to provide a quadratic majorizer for each term in the sum on the right-hand-size of (5.3). ∎

Given that we have constructed quadratic majorizers for $h_f$ and $h_{\psi,\text{Local}}$, the following corollary of Theorem 5.1 derives a quadratic majorizer for the line search function $h$.

Corollary 5.2. *Let* $G_\psi$ *be an operator defined as in Theorem 5.1. Then, the quadratic function*

$$\begin{aligned} g_h(\alpha\,;\bar{\alpha},\boldsymbol{X},\boldsymbol{\Delta},G_\psi) &\triangleq g_{h_f}(\alpha\,;\bar{\alpha},\boldsymbol{X},\boldsymbol{\Delta}) + \beta g_{h_{\psi,\text{Local}}}(\alpha\,;\bar{\alpha},\boldsymbol{X},\boldsymbol{\Delta},G_\psi) \\ &= c^{(0)}_h(\bar{\alpha},\boldsymbol{X},\boldsymbol{\Delta}) + c^{(1)}_h(\bar{\alpha},\boldsymbol{X},\boldsymbol{\Delta})(\alpha-\bar{\alpha}) \\ &\quad + \frac{1}{2}c^{(2)}_h(\bar{\alpha},\boldsymbol{X},\boldsymbol{\Delta},G_\psi)(\alpha-\bar{\alpha})^2, \end{aligned} \tag{5.9, 5.10}$$

*with coefficients given by:*

$$c^{(0)}_h(\bar{\alpha},\boldsymbol{X},\boldsymbol{\Delta}) = c^{(0)}_f(\bar{\alpha},\boldsymbol{X},\boldsymbol{\Delta}) + \beta c^{(0)}_{h_{\psi,\text{Local}}}(\bar{\alpha},\boldsymbol{X},\boldsymbol{\Delta}),$$

$$c^{(1)}_h(\bar{\alpha},\boldsymbol{X},\boldsymbol{\Delta}) = c^{(1)}_f(\bar{\alpha},\boldsymbol{X},\boldsymbol{\Delta}) + \beta c^{(1)}_{h_{\psi,\text{Local}}}(\bar{\alpha},\boldsymbol{X},\boldsymbol{\Delta}), \tag{5.11}$$

$$c^{(2)}_h(\bar{\alpha},\boldsymbol{X},\boldsymbol{\Delta},G_\psi) = c^{(2)}_f(\bar{\alpha},\boldsymbol{X},\boldsymbol{\Delta}) + \beta c^{(2)}_{h_{\psi,\text{Local}}}(\bar{\alpha},\boldsymbol{X},\boldsymbol{\Delta},G_\psi), \tag{5.12}$$

*is a majorizer for* $h(\alpha\,;\boldsymbol{X},\boldsymbol{\Delta})$ *at* $\bar{\alpha}$.

Remark 5.3. *The existence of a majorizer for the line search function* $h$ *given by Corollary 5.2 enables the minimization of* $h$ *using a simple iterative majorize-minimize approach (MM) [19,* ***S*** *IV]. Given an initial guess* $\alpha_0$*, it is straightforward to show that the iterative step*

$$\alpha_{k+1} \triangleq \operatorname*{arg\,min}_{\alpha\in\mathbb{R}} g_h(\alpha\,;\alpha_k,\boldsymbol{X},\boldsymbol{\Delta},G_\psi) = \alpha_k - \frac{c^{(1)}_h(\alpha_k,\boldsymbol{X},\boldsymbol{\Delta})}{c^{(2)}_h(\alpha_k,\boldsymbol{X},\boldsymbol{\Delta},G_\psi)} \tag{5.13}$$

*decreases* $h(\alpha\,;\boldsymbol{X},\boldsymbol{\Delta})$ *monotonically, i.e.,* $h(\alpha_{k+1}\,;\boldsymbol{X},\boldsymbol{\Delta}) \le h(\alpha_k\,;\boldsymbol{X},\boldsymbol{\Delta})$*. Let* $n_\alpha$ *denote the number of iterations of (5.13) that we use to descend* $h(\alpha\,;\boldsymbol{X},\boldsymbol{\Delta})$*.*

To apply the MM step-size selection method in (5.13), one must calculate $c^{(1)}_{h_{\psi,\text{Local}}}$ and $c^{(2)}_{h_{\psi,\text{Local}}}$ as given in (5.7) and (5.8), respectively, which can be computationally demanding because one SVD should be performed for each pair $(\boldsymbol{s},\boldsymbol{p}) \in \Lambda\times\Gamma$. In the following we provide a heuristic fast strategy for this calculation.

**5.1. Fast step-size selection strategy.** Instead of considering every pair $(\boldsymbol{s},\boldsymbol{p}) \in \Lambda \times \Gamma$ for calculating $c^{(1)}_{h_{\psi,\text{Local}}}$ and $c^{(2)}_{h_{\psi,\text{Local}}}$, we have empirically observed that it suffices to use only the pairs associated with a single shift index, denoted $\bar{\boldsymbol{s}} \in \Lambda$, that we typically set to $\boldsymbol{s} = \boldsymbol{0}$ for simplicity. For our fast variant, we approximate the majorizer $g_{h_{\psi,\text{Local}}}(\alpha\,;\bar{\alpha},\boldsymbol{X},\boldsymbol{\Delta},G_\psi)$ by the quadratic function

$$\begin{aligned}\bar{g}_{h_{\psi,\text{Local}}}(\alpha\,;\bar{\alpha},\boldsymbol{X},\boldsymbol{\Delta},G_\psi) \triangleq\ & \bar{c}^{(0)}_{h_{\psi,\text{Local}}}(\bar{\alpha},\boldsymbol{X},\boldsymbol{\Delta}) + \bar{c}^{(1)}_{h_{\psi,\text{Local}}}(\bar{\alpha},\boldsymbol{X},\boldsymbol{\Delta})\,(\alpha-\bar{\alpha}) \\ & + \frac{1}{2}\bar{c}^{(2)}_{h_{\psi,\text{Local}}}(\bar{\alpha},\boldsymbol{X},\boldsymbol{\Delta},G_\psi)\,(\alpha-\bar{\alpha})^2,\end{aligned} \tag{5.14}$$

with coefficients given by:

$$\begin{aligned}\bar{c}^{(0)}_{h_{\psi,\text{Local}}}(\bar{\alpha},\boldsymbol{X},\boldsymbol{\Delta}) &= |\Lambda| \sum_{\boldsymbol{p}\in\Gamma} c^{(0)}_{h_\psi}(\bar{\alpha},\boldsymbol{X}^{(\boldsymbol{p},\bar{\boldsymbol{s}})},\boldsymbol{\Delta}^{(\boldsymbol{p},\bar{\boldsymbol{s}})}),\\ \bar{c}^{(1)}_{h_{\psi,\text{Local}}}(\bar{\alpha},\boldsymbol{X},\boldsymbol{\Delta}) &= |\Lambda| \sum_{\boldsymbol{p}\in\Gamma} c^{(1)}_{h_\psi}(\bar{\alpha},\boldsymbol{X}^{(\boldsymbol{p},\bar{\boldsymbol{s}})},\boldsymbol{\Delta}^{(\boldsymbol{p},\bar{\boldsymbol{s}})}),\\ \bar{c}^{(2)}_{h_{\psi,\text{Local}}}(\bar{\alpha},\boldsymbol{X},\boldsymbol{\Delta},G_\psi) &= |\Lambda| \sum_{\boldsymbol{p}\in\Gamma} c^{(2)}_{h_\psi}(\bar{\alpha},\boldsymbol{X}^{(\boldsymbol{p},\bar{\boldsymbol{s}})},\boldsymbol{\Delta}^{(\boldsymbol{p},\bar{\boldsymbol{s}})},G_\psi).\end{aligned}$$

This subsequently provides an approximation for the majorizer $g_h(\alpha\,;\bar{\alpha},\boldsymbol{X},\boldsymbol{\Delta},G_\psi)$ given by the quadratic function

$$\begin{aligned}\bar{g}_h(\alpha\,;\bar{\alpha},\boldsymbol{X},\boldsymbol{\Delta},G_\psi) &\triangleq g_{h_f}(\alpha\,;\bar{\alpha},\boldsymbol{X},\boldsymbol{\Delta}) + \beta\bar{g}_{h_{\psi,\text{Local}}}(\alpha\,;\bar{\alpha},\boldsymbol{X},\boldsymbol{\Delta},G_\psi)\\ &= \bar{c}^{(0)}_h(\bar{\alpha},\boldsymbol{X},\boldsymbol{\Delta}) + \bar{c}^{(1)}_h(\bar{\alpha},\boldsymbol{X},\boldsymbol{\Delta})\,(\alpha-\bar{\alpha})\\ &\quad + \frac{1}{2}\bar{c}^{(2)}_h(\bar{\alpha},\boldsymbol{X},\boldsymbol{\Delta},G_\psi)\,(\alpha-\bar{\alpha})^2,\end{aligned}$$

with coefficients given by:

$$\begin{aligned}\bar{c}^{(0)}_h(\bar{\alpha},\boldsymbol{X},\boldsymbol{\Delta}) &= c^{(0)}_f(\bar{\alpha},\boldsymbol{X},\boldsymbol{\Delta}) + \beta\bar{c}^{(0)}_{h_{\psi,\text{Local}}}(\bar{\alpha},\boldsymbol{X},\boldsymbol{\Delta}),\\ \bar{c}^{(1)}_h(\bar{\alpha},\boldsymbol{X},\boldsymbol{\Delta}) &= c^{(1)}_f(\bar{\alpha},\boldsymbol{X},\boldsymbol{\Delta}) + \beta\bar{c}^{(1)}_{h_{\psi,\text{Local}}}(\bar{\alpha},\boldsymbol{X},\boldsymbol{\Delta}),\\ \bar{c}^{(2)}_h(\bar{\alpha},\boldsymbol{X},\boldsymbol{\Delta},G_\psi) &= c^{(2)}_f(\bar{\alpha},\boldsymbol{X},\boldsymbol{\Delta}) + \beta\bar{c}^{(2)}_{h_{\psi,\text{Local}}}(\bar{\alpha},\boldsymbol{X},\boldsymbol{\Delta},G_\psi).\end{aligned}$$

Then, instead of using (5.13), we use the iterative step

$$\alpha_{k+1} \triangleq \operatorname*{arg\,min}_{\alpha\in\mathbb{R}} \bar{g}_h(\alpha\,;\alpha_k,\boldsymbol{X},\boldsymbol{\Delta},G_\psi) = \alpha_k - \frac{\bar{c}^{(1)}_h(\alpha_k,\boldsymbol{X},\boldsymbol{\Delta})}{\bar{c}^{(2)}_h(\alpha_k,\boldsymbol{X},\boldsymbol{\Delta})}. \tag{5.15}$$

This heuristic approach is substantially faster than the one in (5.13) as only one SVD is performed instead of $|\Lambda||\Gamma|$; however, a step size produced with this method is not guaranteed to decrease $h(\alpha\,;\boldsymbol{X},\boldsymbol{\Delta})$ monotonically, as $\bar{g}_h(\alpha\,;\bar{\alpha},\boldsymbol{X},\boldsymbol{\Delta},G_\psi)$ is not necessarily a majorizer for $h(\alpha\,;\boldsymbol{X},\boldsymbol{\Delta})$. We have empirically seen that $\bar{g}_h(\alpha\,;\bar{\alpha},\boldsymbol{X},\boldsymbol{\Delta},G_\psi)$ resembles $g_h(\alpha\,;\bar{\alpha},\boldsymbol{X},\boldsymbol{\Delta},G_\psi)$ quite well, and does not considerably affect performance when estimating $\boldsymbol{X}$. Intuitively, the

good performance of this method could be attributed to some isotropy of the locally low-rank regularizer, in the sense that every shift $\boldsymbol{s} \in \Lambda$ contributes similarly to the cost function.

The following section shows empirically how the gradient formula in (5.1) and the step-size iterative selection strategy in (5.13) allow the minimization of $\Psi_{\text{Local}}$ using standard iterative gradient-based optimization algorithms. We illustrate this procedure in the context of dynamic MRI reconstruction.

**6. Application in dynamic MRI reconstruction using locally low-rank constraints.** In dynamic MRI applications it is typical to acquire a limited amount of samples to accelerate the acquisition, as data collection is inherently slow in MRI. Overall, the main goal is to reconstruct a series of images from a partial set of samples that have also been corrupted by noise. In the following we assume that these images are 2D, although our analysis can be easily extended to higher dimensions. Mathematically, the data-collection process is usually modeled as:

$$\boldsymbol{Y} = \mathcal{A}(\boldsymbol{X}) + \boldsymbol{E} \in \mathbb{C}^{S \times N}, \tag{6.1}$$

where $\boldsymbol{X} = \begin{bmatrix} \boldsymbol{x}_1 & \boldsymbol{x}_2 & \cdots & \boldsymbol{x}_N \end{bmatrix} \in \mathbb{C}^{M \times N}$ is a matrix whose columns $\{\boldsymbol{x}_n\}_{n=1}^N$ are the (vectorized) images to be recovered; $\boldsymbol{Y} = \begin{bmatrix} \boldsymbol{y}_1 & \boldsymbol{y}_2 & \cdots & \boldsymbol{y}_N \end{bmatrix} \in \mathbb{C}^{S \times N}$ is a matrix whose columns $\{\boldsymbol{y}_n\}_{n=1}^N$ are the observed data samples in the Fourier domain (a.k.a. k-space) for each image; $\boldsymbol{E}$ is a matrix that represents the noise in the observations[7]; and $\mathcal{A} : \mathbb{C}^{M \times N} \to \mathbb{C}^{S \times N}$ is the linear forward operator that represents the MRI acquisition process[8]. The acquisition of a limited amount of samples is modeled by including an undersampling matrix in $\mathcal{A}$. This makes recovering $\boldsymbol{X}$ from $\boldsymbol{Y}$ an ill-posed inverse problem. One option to recover $\boldsymbol{X}$ is by minimizing a data-consistency cost function of the form:

$$f(\boldsymbol{X}) \triangleq \frac{1}{2} \left\| \mathcal{A}(\boldsymbol{X}) - \boldsymbol{Y} \right\|_{\text{F}}^2, \tag{6.2}$$

which can be done using well-known least-squares solvers; however, additional regularizers are needed in cases when data are heavily undersampled. In the following we study how to estimate $\boldsymbol{X}$ when locally low-rank regularizers are added by using the proposed smooth optimization framework from Section 5. We start by describing how the locally low-rank model introduced in (1.2) and (1.5) is applied in the context of dynamic MRI reconstruction.

The underlying assumption for the use of locally low-rank models is that patches extracted from the same spatial locations across images should be similar. More specifically, if $\boldsymbol{p} \in \mathbb{Z}^2$ corresponds to the spatial location of one specific voxel, it is then possible to extract from each image the values in a neighborhood around $\boldsymbol{p}$ corresponding to a patch of dimensions $n_x \times n_y$. In our examples we used rectangular neighborhoods and we denote by $P = n_x n_y$ the number of voxels in each of them. Another possibility is to use ellipsoidal neighborhoods [44]. Then, low-rank characteristics are expected for the matrix constructed by concatenating the vectorized patches corresponding to $\boldsymbol{p}$ from the different images. This matrix has a Casorati

[7] The entries in $\boldsymbol{E}$ are usually modeled as independent identically distributed variables following a white Gaussian complex distribution [41].

[8] See [13] for a detailed explanation of $\mathcal{A}$. In general terms, $\mathcal{A}$ involves multiplication with coil-sensitivities, Fourier transformation, and an undersampling process.

structure and we denote it by $\mathcal{P}_{\boldsymbol{p}}(\boldsymbol{X})$, where $\mathcal{P}_{\boldsymbol{p}} : \mathbb{C}^{M\times N} \to \mathbb{C}^{P\times N}$ is the linear operator that performs the Casorati matrix construction for the patch corresponding to $\boldsymbol{p}$. The adjoint operator $\mathcal{P}_{\boldsymbol{p}}^* : \mathbb{C}^{P\times N} \to \mathbb{C}^{M\times N}$ constructs a matrix that is zero everywhere, except for the entries corresponding to the patch $\boldsymbol{p}$ which are filled according to the entries of the input. Figure 2 illustrates how $\mathcal{P}_{\boldsymbol{p}}$ and $\mathcal{P}_{\boldsymbol{p}}^*$ perform their respective matrix construction for a series of three images. Locally low-rank models aim to leverage on the low-rank characteristics of the Casorati matrices constructed from multiple patches at different spatial locations. As in (1.2) and (1.5), we denote the set of spatial locations by $\Gamma$, and in our experiments we design it such that the patches corresponding to different spatial locations jointly cover the whole voxel grid while not overlapping with each other. However, one important consideration for locally low-rank models to properly work, is that the patches should overlap to avoid blocky artifacts in the reconstructed images [56]. One way to impose this is by considering the patch extraction process for circularly shifted versions of the image. If $\boldsymbol{s} \in \mathbb{Z}^2$ denotes a shift index, then it is expected that the matrix $\mathcal{P}_{\boldsymbol{p}}(\mathcal{S}_{\boldsymbol{s}}(\boldsymbol{X}))$ would possess low-rank characteristics, where $\mathcal{S}_{\boldsymbol{s}} : \mathbb{C}^{M\times N} \to \mathbb{C}^{M\times N}$ is the linear operator that performs the circular shift by $\boldsymbol{s}$. The adjoint operator $\mathcal{S}_{\boldsymbol{s}}^* : \mathbb{C}^{M\times N} \to \mathbb{C}^{M\times N}$ performs a circular shift by $-\boldsymbol{s}$. The number of shifts that we considered depended on the number of voxels in each patch. If each patch is considered as a 2D grid, then each location in the grid provides a shift index. Let $\Lambda$ denote the set of shifts that also includes $\boldsymbol{s} = [0, 0]^T$ (*i.e.*, no shift), so that $|\Lambda| = n_x n_y$ if $n_x$ and $n_y$ are both even, which is the case considered in our experiments. More specifically,

$$\Lambda \triangleq \left\{ \boldsymbol{s} = [s_x, s_y]^T \;;\; s_x \in \left[-\frac{n_x}{2}+1, \frac{n_x}{2}\right],\; s_y \in \left[-\frac{n_y}{2}+1, \frac{n_y}{2}\right] \right\}. \tag{6.3}$$

Figure 3 illustrates how the shifting operation is combined with patch extraction using the same toy example as in Fig. 2. Under this setting, we propose to estimate $\boldsymbol{X}$ by solving (1.5) using standard iterative gradient-based optimization algorithms by using the results in (5.1) and (5.13). As indicated in Section 5, we first must calculate $\nabla f(\boldsymbol{X})$ and a quadratic majorizer for $h_f(\alpha\,; \boldsymbol{X}, \boldsymbol{\Delta})$. Given the quadratic structure of $f$ in (6.2) it follows that:

$$\nabla f(\boldsymbol{X}) = \mathcal{A}^*(\mathcal{A}(\boldsymbol{X}) - \boldsymbol{Y}), \tag{6.4}$$

and that the coefficients of the quadratic majorizer in (5.5) are given by:

$$\begin{aligned} c_f^{(0)}(\bar{\alpha}, \boldsymbol{X}, \boldsymbol{\Delta}) &= \frac{1}{2}\left\|\mathcal{A}(\boldsymbol{X} + \bar{\alpha}\boldsymbol{\Delta}) - \boldsymbol{Y}\right\|_{\mathrm{F}}^2, \\ c_f^{(1)}(\bar{\alpha}, \boldsymbol{X}, \boldsymbol{\Delta}) &= \mathrm{real}\{\langle \nabla\mathcal{A}(\boldsymbol{X} + \bar{\alpha}\boldsymbol{\Delta}) - \boldsymbol{Y},\, \mathcal{A}(\boldsymbol{\Delta})\rangle\}, \\ c_f^{(2)}(\boldsymbol{\Delta}) &= \left\|\mathcal{A}(\boldsymbol{\Delta})\right\|_{\mathrm{F}}^2. \end{aligned}$$

Using the gradient calculation results in (2.9), (5.1), and (6.4), in addition to the MM step-size selection strategy in (5.13) or its fast (heuristic) version in (5.15), we use a method like NCG to solve (1.5). In the following we show experiments using this optimization approach and dynamic MRI data.

**6.1. Experiments.** In this section we test the proposed optimization framework by reconstructing realistic retrospectively undersampled dynamic MRI data. We studied imposing

locally low-rank models using the Huber-based low-rank regularizer $R_\psi$ and its tail version $R_{\psi,K}$. The standard iterative gradient-based algorithm used in our experiments was NCG. Appendix J provides pseudocode and further details for the NCG implementation. NCG was compared with ad-hoc heuristic versions of two proximal gradients methods: POGM and FISTA. For these two proximal gradient methods the cost function was the one in (1.2). Since the locally low-rank regularizer is not prox friendly, for both POGM and FISTA we *approximated* the proximal mapping for the regularizer using the average of the proximal mappings of each term inside the sum (a.k.a. a proximal average [1]).

**6.1.1. Data description and forward operator.** The data used in our experiments corresponded to a 2D cardiac perfusion dataset of size $128 \times 128$ (*i.e.*, $M = 16384$) with $N = 40$ time frames [51]. In this case we have data from 12 coils; therefore, the forward operator $\mathcal{A}$ includes multiplication with coil-sensitivities, Fourier transformation, and undersampling in the k-space corresponding to each time frame. The multicoil k-space data corresponding to each time frame was undersampled to obtain a $\times 7$-accelerated dataset. The undersampling scheme guaranteed that each k-space sample was present at least once when considering all time frames.

**6.1.2. Optimization framework parameters.** To use the proposed optimization framework we first needed a Huber potential function $\psi$ such that $R_\psi$ and $R_{\psi,K}$ were able to impose low-rank models. We focused our analysis on the (convex) hyperbola function defined in (1.6) for $\delta = 10^{-3}$, as $R_\psi$ and $R_{\psi,K}$ in this case can be seen as smooth versions of the nuclear norm (*cf.* Fig. 1.a) and the regularizer corresponding to the sum of the tail singular values [49], respectively; however, we also provide some results using the (non-convex) Cauchy potential function defined in (2.6). In all of our experiments we set $K = 1$ for $R_{\psi,K}$. To use the MM step-size selection strategy in (5.13) we studied $G_\psi = G_\psi^{\mathrm{R}}$ and $G_\psi = G_\psi^{\mathrm{L}}$ when using $R_\psi$, as both provide valid quadratic majorizers according to Corollary 3.3. For $R_{\psi,K}$ we used the analogous operators $G_{\psi,\boldsymbol{w}} = G_{\psi,\boldsymbol{w}_K}^{\mathrm{R}}$ and $G_{\psi,\boldsymbol{w}} = G_{\psi,\boldsymbol{w}_K}^{\mathrm{L}}$ defined in Appendix H. We set the number of iterations for the MM step-size selection strategy to $n_\alpha = 1$ and the initial step size as $\alpha_0 = 0$. In cases where the (heuristic) fast step-size selection strategy was used we set $\bar{\boldsymbol{s}} = [0, 0]^T$. The operator $\mathcal{P}_{\boldsymbol{p}}$ was designed to extract $8 \times 8$ patches (*i.e.*, $n_x = n_y = 8$), and we selected $\Gamma$ such that the $128 \times 128$ grid of voxels could be completely covered using non-overlapping patches before applying the shifting operator. Thus, $|\Gamma| = (128/n_x)(128/n_y) = 256$ in this example, and $|\Lambda| = n_x n_y = 64$. Each method was initialized using a data-sharing reconstruction [29] where each time frame was reconstructed by filling missing k-space samples using available k-space samples in neighboring time frames. Each method was run for 500 iterations and implemented in-house using MATLAB R2023a. All computations were performed on a MacBook Pro laptop computer with an Apple M2 Pro chip, 12 cores, and 32GB RAM. The authors have made an open-source implementation available at https://github.com/ralobos/smooth_LLR.

**6.1.3. Performance metrics.** To study the convergence rate of each method we calculated the normalized distance to the limit

$$\frac{\|\boldsymbol{X}_k - \hat{\boldsymbol{X}}_\infty\|_{\mathrm{F}}}{\|\hat{\boldsymbol{X}}_\infty\|_{\mathrm{F}}} \tag{6.5}$$

at each iteration, where $\boldsymbol{X}_k$ was the estimate at the $k$th iteration and $\hat{\boldsymbol{X}}_\infty$ was the estimate after 500 iterations. To measure reconstruction quality we calculated the normalized-root-mean-square-error (NRMSE) at each iteration defined as

$$\frac{\|\boldsymbol{X}_k - \boldsymbol{X}_{\mathrm{GS}}\|_{\mathrm{F}}}{\|\boldsymbol{X}_{\mathrm{GS}}\|_{\mathrm{F}}}, \tag{6.6}$$

where $\boldsymbol{X}_{\mathrm{GS}}$ corresponded to the gold-standard reconstruction obtained after coil-combination of the fully sampled data using a SENSE-based approach [52].

**6.2. Results.** Figure 4 shows the measures in (6.5) and (6.6) for each method. In Fig. 4.a NCG converged faster than the other two methods, using either $R_\psi$ or $R_{\psi,K}$, and POGM converged faster than FISTA. The faster convergence of POGM compared to FISTA was also observed for global low-rank models [42]. NCG using $R_\psi$ yielded similar NRMSE values as POGM, while taking fewer iterations for NCG to converge. NCG using $R_{\psi,K}$ obtained a better NRMSE than POGM at the point of convergence, and converged the fastest. The convergence of NCG is theoretically ensured [21] whereas the convergence of POGM and FISTA and their point of convergence are unclear in this context because of the heuristic approximation of the proximal mapping in both cases. NCG using the tail regularizer $R_{\psi,K}$ converged faster and obtained better image quality than NCG using the non-weighted regularizer $R_\psi$ as expected, because the tail regularizer exploits a priori estimate of the true rank and penalizes only tail singular values.

Although NCG converged faster than POGM and FISTA, it was the most computationally expensive, as many SVD calculations were needed for the MM step-size selection strategy in (5.13). For this reason we also explored the heuristic step-size selection strategy proposed in (5.15). Figure 5 shows NCG results using $R_\psi$ and both step-size selection strategies. Neither convergence nor NRMSE were considerably affected when adopting the fast (heuristic) step-size selection strategy (similar results were obtained for NCG using $R_{\psi,K}$). The heuristic step-size selection did not visibly affect the quality of the reconstructed images either. Figure 6 shows examples of the reconstructed images obtained with each method using only 25 iterations in each case. Using the heuristic (fast) step-size selection strategy did not cause visible changes. However, the fast step-size strategy significantly reduced NCG compute time as shown in Table 1 that reports the median times in all cases after repeating each experiment five times. Only the results for $G_\psi^{\mathrm{R}}$ and $G_{\psi,\boldsymbol{w}_K}^{\mathrm{R}}$ are shown, as no substantial differences were observed when using $G_\psi^{\mathrm{L}}$ and $G_{\psi,\boldsymbol{w}_K}^{\mathrm{L}}$ instead. To further study the similarities between the two step-size selection strategies in terms of convergence and image quality, we calculated the quadratic functions $g_{h_{\psi,\mathrm{Local}}}$ and $\bar{g}_{h_{\psi,\mathrm{Local}}}$ for one particular NCG iteration using (5.6) and (5.14), respectively, as they represent the main difference between the two strategies. Denoting the estimation and search direction for this iteration as $\boldsymbol{X}_k$ and $\boldsymbol{\Delta}_k$, respectively, Fig. 7.a shows: $h_{\psi,\mathrm{Local}}(\alpha; \boldsymbol{X}_k, \boldsymbol{\Delta}_k)$ calculated for different values of $\alpha$; $g_{h_{\psi,\mathrm{Local}}}(\alpha\,; \bar{\alpha}, \boldsymbol{X}_k, \boldsymbol{\Delta}_k, G_\psi)$ and $\bar{g}_{h_{\psi,\mathrm{Local}}}(\alpha\,; \bar{\alpha}, \boldsymbol{X}_k, \boldsymbol{\Delta}_k, G_\psi)$ when $\bar{\alpha} = 0$ and $G_\psi = G_\psi^{\mathrm{R}}$ or $G_\psi = G_\psi^{\mathrm{L}}$. As indicated by our theoretical results in Theorem 5.1, $g_{h_{\psi,\mathrm{Local}}}(\alpha\,; \bar{\alpha}, \boldsymbol{X}_k, \boldsymbol{\Delta}_k, G_\psi)$ majorizes $h_{\mathrm{Local}}(\alpha; \boldsymbol{X}_k, \boldsymbol{\Delta}_k)$ at every $\alpha$ and they are equal at $\bar{\alpha}$, both for $G_\psi = G_\psi^{\mathrm{R}}$ or $G_\psi = G_\psi^{\mathrm{L}}$. Notably, $\bar{g}_{h_{\psi,\mathrm{Local}}}(\alpha\,; \bar{\alpha}, \boldsymbol{X}_k, \boldsymbol{\Delta}_k, G_\psi)$ resembled $g_{h_{\psi,\mathrm{Local}}}(\alpha\,; \bar{\alpha}, \boldsymbol{X}_k, \boldsymbol{\Delta}_k, G_\psi)$ quite well for each choice of $G_\psi$, providing further explanation for why choosing the heuristic step-size selection strategy did not affect convergence

nor estimation quality. Analogous results are observed in Fig. 7.b when using the tail regularizer, although in this case the quadratic functions were calculated based on $G^{\mathrm{R}}_{\psi,\boldsymbol{w}_K}$ and $G^{\mathrm{L}}_{\psi,\boldsymbol{w}_K}$. For completeness, Fig. 7.c shows an analogous analysis using the Cauchy function as the potential function for $R_\psi$. In this case $h_{\psi,\mathrm{Local}}(\alpha; \boldsymbol{X}_k, \boldsymbol{\Delta}_k)$ has a challenging non-convex behavior; however, it can still be minimized using the proposed strategy based on quadratic majorizers. Figure 7.a shows that $G^{\mathrm{R}}_\psi$ provided better majorizing characteristics than $G^{\mathrm{L}}_\psi$, as the global minimum of $h_{\psi,\mathrm{Local}}(\alpha; \boldsymbol{X}_k, \boldsymbol{\Delta}_k)$ was closer to the global minimum of $g_{h_{\psi,\mathrm{Local}}}(\alpha\ ; \bar{\alpha}, \boldsymbol{X}_k, \boldsymbol{\Delta}_k, G^{\mathrm{R}}_\psi)$ than the global minimum of $g_{h_{\psi,\mathrm{Local}}}(\alpha\ ; \bar{\alpha}, \boldsymbol{X}_k, \boldsymbol{\Delta}_k, G^{\mathrm{L}}_\psi)$. This is consistent with the theoretical results in Corollary 3.3. However, the results in Fig. 4 and Fig. 5 illustrate that the differences between the majorizers associated with $G^{\mathrm{R}}_\psi$ and $G^{\mathrm{L}}_\psi$ did not have a big impact when minimizing the cost function in (1.5). This can be attributed to the fact that the data-consistency term given by $f$ had a bigger contribution in our experiments than the regularizer. As a consequence, the function $g_f$ dominated over $g_{h_{\psi,\mathrm{Local}}}$ when calculating $g_h$ in (5.9) to majorize the line search function $h$, which mitigated the effects of using $G^{\mathrm{L}}_\psi$ instead of $G^{\mathrm{R}}_\psi$.

Table 1: Reconstruction time after 25 iterations.

| **Method** | **Time [secs]** | **NRMSE** |
|---|---|---|
| POGM | 35.1 | 0.138 |
| NCG ($G^{\mathrm{R}}_\psi$) | 75.9 | 0.141 |
| NCG ($G^{\mathrm{R}}_{\psi,\boldsymbol{w}_K}$, Tail) | 76 | 0.136 |
| NCG ($G^{\mathrm{R}}_\psi$ ) - Fast step size | 39 | 0.141 |
| NCG ($G^{\mathrm{R}}_{\psi,\boldsymbol{w}_K}$, Tail) - Fast step size | 38.9 | 0.136 |

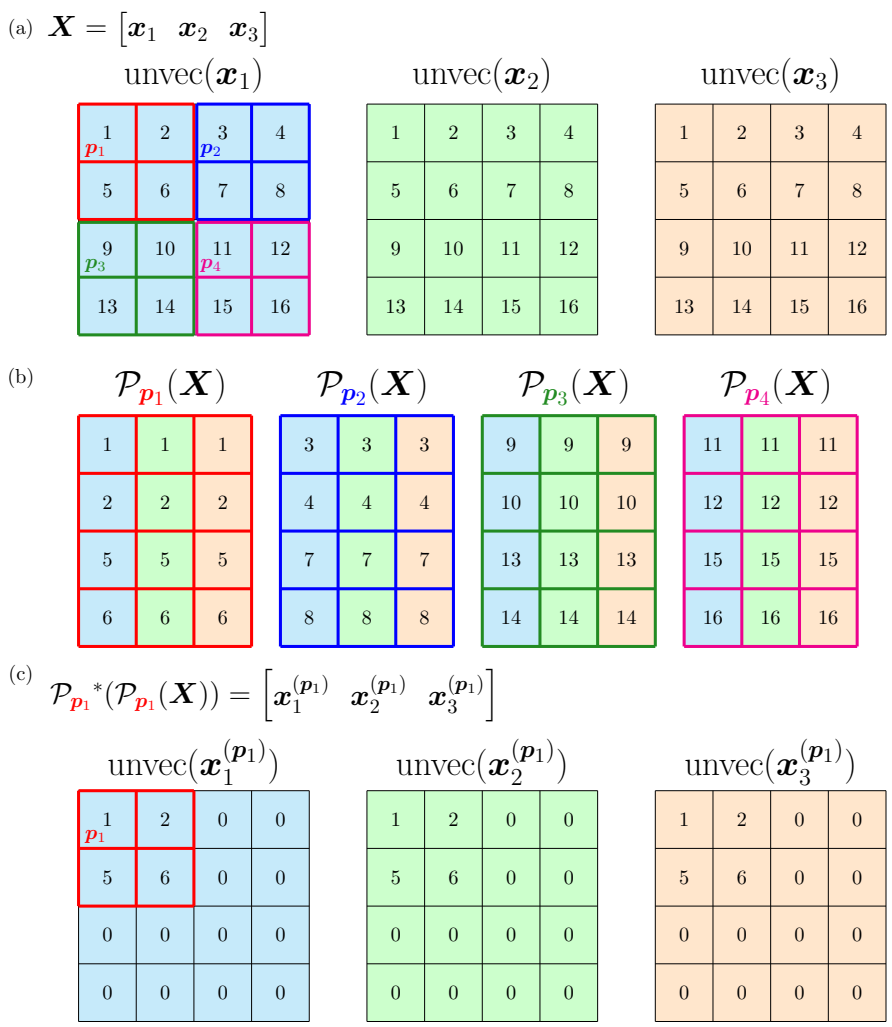


Figure 2: Illustration of the operators $\mathcal{P}_{\boldsymbol{p}}$ and $\mathcal{P}^*_{\boldsymbol{p}}$ for a series of $N = 3$ 2D-images with $M = 16$ voxels each. (a) shows each image (*i.e.*, the columns of $\boldsymbol{X}$) as a 2D grid after unvectorizing the corresponding column in $\boldsymbol{X}$; the value of each voxel is indicated in black at the center of each square of the grid. Each image has been filled out with a different color (light blue, light green, and light orange) to identify how the voxels are taken from each image once the Casorati matrices are constructed. The set of locations $\Gamma = \{\boldsymbol{p}_1, \boldsymbol{p}_2, \boldsymbol{p}_3, \boldsymbol{p}_4\}$ has been indicated in the first image using a color code; the same locations are used in the other two images. (b) shows the Casorati matrices created after extracting the patches corresponding to the locations in $\Gamma$. A grid with the same color of the location index has been used for each Casorati matrix. This should help the reader to identify which voxels were taken from each image to construct the Casorati matrices, as the same grid color has been used in (a) to indicate the neighborhood of voxels that forms the patch corresponding to each location. In this example the dimensions of each patch were $n_x \times n_y = 2 \times 2$ (*i.e.*, $P = 4$). (c) shows an example of how $\mathcal{P}^*_{\boldsymbol{p}}$ performs its matrix construction. The columns of $\mathcal{P}^*_{\boldsymbol{p}_1}(\mathcal{P}_{\boldsymbol{p}_1}(\boldsymbol{X}))$, denoted by $\{\boldsymbol{x}_n^{(\boldsymbol{p}_1)}\}_{n=1}^3$, are shown after unvectorization.

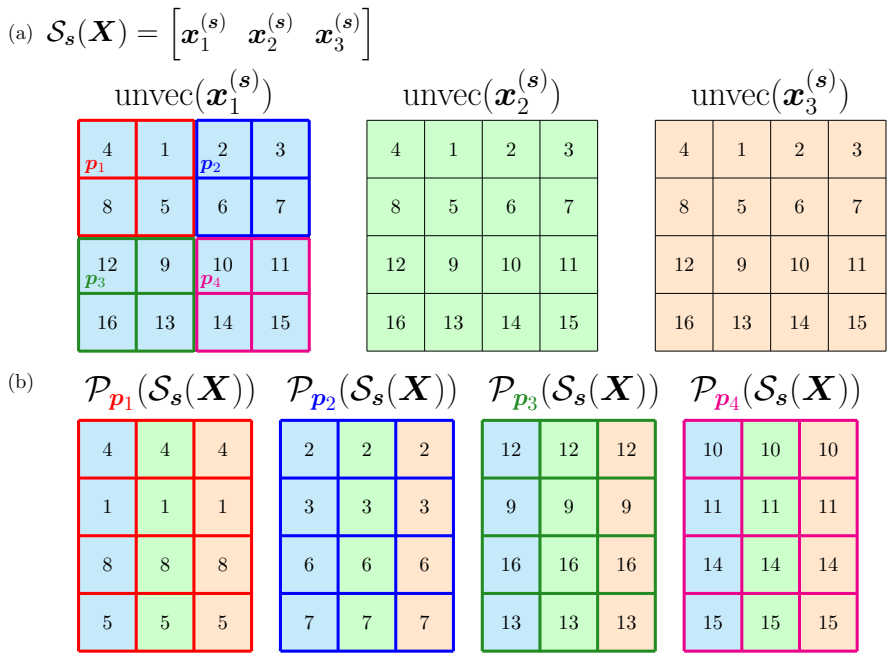


Figure 3: Illustration of the shifting operator using the same images and color code used in Fig. 2. (a) shows how each column of $\boldsymbol{X}$ is modified after applying the operator $\mathcal{S}_{\boldsymbol{s}}$ when $\boldsymbol{s} = [1, 0]^T$. The modified columns are denoted by $\{\boldsymbol{x}_n^{(\boldsymbol{s})}\}_{n=1}^3$, and correspond to the vectorized images after circularly shifting the images according to $\boldsymbol{s}$. The first and second entries of $\boldsymbol{s}$ indicate how many positions each voxel should be shifted horizontally and vertically, respectively; in this example $\boldsymbol{s}$ indicates one position to the right and no vertical shifts. The total number of shift vectors depends on the number of voxels in each patch. In this case $\Lambda = \{[0, 0]^T, [0, 1]^T, [1, 0]^T, [1, 1]^T\}$ according to (6.3). (b) shows the Casorati matrices created after extracting the patches corresponding to the locations in $\Gamma$ as done in Fig. 2.b, after circularly shifting the images according to $\boldsymbol{s}$.

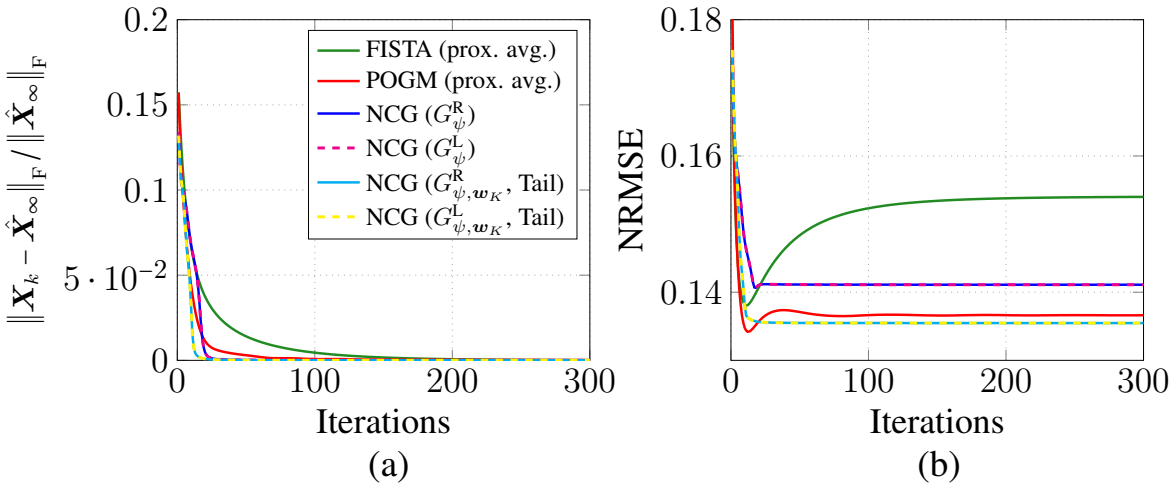


Figure 4: Convergence and NRMSE metrics for each method as functions of the number of iterations (only 300 of the 500 iterations are shown). In both plots NCG using $R_\psi$ corresponds to NCG($G^{\mathrm{R}}_{\psi}$) and NCG($G^{\mathrm{L}}_{\psi}$), and NCG using $R_{\psi,K}$ corresponds to NCG($G^{\mathrm{R}}_{\psi,\boldsymbol{w}_K}$, Tail) and NCG($G^{\mathrm{L}}_{\psi,\boldsymbol{w}_K}$, Tail). The operator in parenthesis is the one used for the MM step-size selection strategy in (5.13). For POGM and FISTA we have indicated in parenthesis that proximal average has been used as an approximation of the proximal mapping.

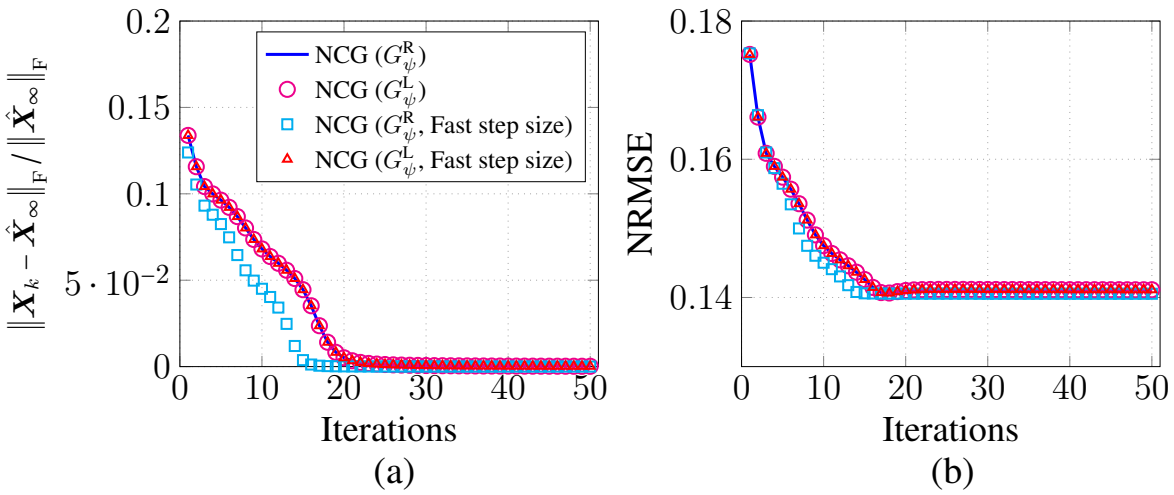


Figure 5: Convergence and NRMSE metrics for NCG using $R_\psi$ with different MM step-size selection strategies as functions of the number of iterations (only 50 of the 500 iterations are shown). We indicate using the heuristic step-size selection strategy by writing "Fast step size".

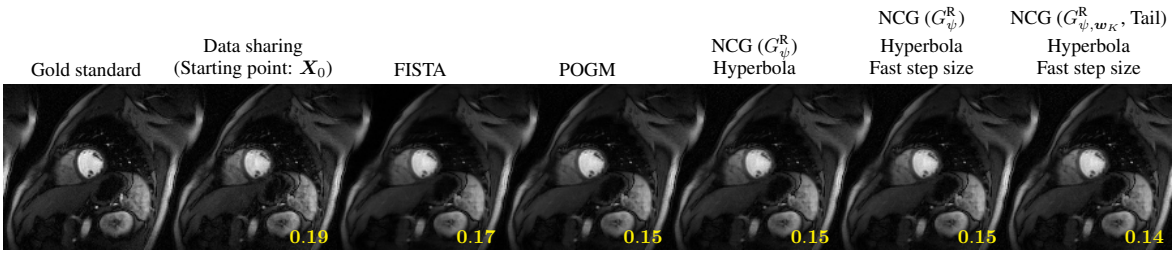


Figure 6: Reconstruction results for different methods using only 25 iterations. Only one image corresponding to one specific time frame is shown for each method, and the NRMSE for that particular image is indicated in yellow in the bottom right corner. For NCG using $R_\psi$ results are shown using both step-size selection strategies for a visual comparison between them. For NCG using $R_{\psi,K}$ only the reconstruction using the heuristic (fast) step-size selection strategy is shown, as no substantial differences were observed compared to using the non-heuristic version. We indicated use of the heuristic step-size selection strategy by writing "Fast step size". Similar results were obtained for NCG when using $G_\psi^L$ instead of $G_\psi^R$, and $G_{\psi,\boldsymbol{w}_K}^L$ instead of $G_{\psi,\boldsymbol{w}_K}^R$ (not shown).

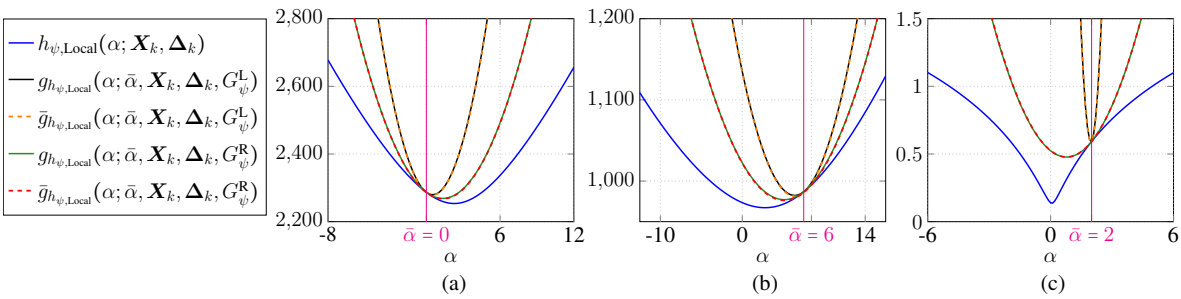


Figure 7: Illustration of the proposed quadratic majorizers for $h_{\psi,\text{Local}}$ given in Theorem 5.1 when using (a) $R_\psi$ with $\psi$ as the hyperbola function, (b) $R_{\psi,K}$ with $\psi$ as the hyperbola function, and (c) $R_\psi$ with $\psi$ as the Cauchy function. We also show the approximation of each quadratic majorizer (dashed lines) as defined in (5.14). Different values of $\bar{\alpha}$ are used in each case to illustrate different examples of our theoretical results. When using the tail regularizer the function $h_{\psi,\text{Local}}$ is defined in terms of $R_{\psi,K}$, and the quadratic majorizers and their approximations are calculated considering the operators $G_{\psi,\boldsymbol{w}_K}^R$ and $G_{\psi,\boldsymbol{w}_K}^L$ (*cf.* Appendix H).

**7. Discussion and conclusion.** In this work we have proposed new classes of smooth regularizers to impose either global or locally low-rank models in inverse problems. We have studied several properties of these regularizers using singular value function theory, establishing conditions for their convexity, differentiability, and Lipschitz continuity of the gradient. We have also provided novel theory that enables the construction of majorizers for the proposed regularizers, which corresponds to one of our main theoretical contributions. Moreover, we have shown that these regularizers enable the use of standard iterative gradient-based optimization methods to solve inverse problems using low-rank models. For this purpose, we have shown how to calculate the regularizer gradient in closed-form, and also how to efficiently select the step-size in each iteration using a majorize-minimize strategy based on quadratic majorizers of the regularizer line search function.

Another point to highlight is the flexibility offered by the proposed theoretical framework, in the sense that a big family of low-rank regularizers can be analyzed using the same theoretical results. Many Huber-like potential functions have been proposed and each of them would provide a regularizer according to our theory. Interestingly, some of these Huber-based low-rank regularizers can be considered smooth versions of commonly used non-smooth low-rank regularizers. For example, the nuclear norm can be approximated by selecting a potential function like the hyperbola function that approximates the absolute value function, and non-convex Schatten-$p$ quasi-norms with $0 < p < 1$ can be approximated by selecting the potential function to be $\psi(t) = (|t|^2 + \delta^2)^{p/2}$ for a small value of $\delta$. This same principle holds for the proposed smooth weighted Huber-based low-rank regularizers (*cf.* Section 4). Remarkably, the proposed optimization framework enables the minimization of each Huber-based low-rank regularizer using the same iterative gradient-based optimization algorithm.

As an application, we showed that the proposed optimization framework based on smooth low-rank regularizers can be used to address the dynamic MRI reconstruction problem when using locally low-rank models with overlapping patches. Particularly, we showed that NCG can be used to minimize the associated cost function. NCG showed a faster convergence and similar or better image quality than other heuristic ad-hoc proximal methods that use the nuclear norm as a regularizer. Moreover, methods like NCG provide well-known convergence guarantees [21] that are not available for proximal methods with approximate proximal maps in this context. In addition, we have observed (not shown) that quasi-Newton methods like L-BFGS can also be used instead of NCG, providing similar reconstruction quality.

As future work we would like to explore other applications for the proposed tail Huber-based low-rank regularizers studied in Section 4.1. Interestingly, by selecting the Huber potential function as the hyperbola function, the proposed regularizer can be seen as a smooth version of the regularizer corresponding to the sum of the tail singular values, which has been used in robust PCA applications [6, 49]. Similarly, by selecting the Huber potential function as the parabola, this type of regularizer coincides with the regularizer proposed in [22], which has been extensively used in MRI reconstruction applications using structured low-rank models [4, 24, 32, 45]. The theory and optimization framework proposed in this work could allow a complementary analysis for these applications.

From a theoretical point of view a relevant question is whether "better" majorizers can be constructed for the proposed regularizers. The majorizer $Q(\boldsymbol{X}; \boldsymbol{S}, G_\psi)$ proposed in (3.3) depends on the operator $G_\psi$, and Theorem 3.1 shows that two choices for this operator provide

valid majorizers. However, we have not studied if these majorizers satisfy any optimality criterion. Inspired by the criterion used to study the optimality of quadratic majorizers for Huber potential functions [26, p. 186], we would like to study the existence and construction of an operator $G_\psi^*$ such that:

(i) $Q(\boldsymbol{X}; \boldsymbol{S}, G_\psi^*)$ is a valid majorizer for $R_\psi$ and,

(ii) $Q(\boldsymbol{X}; \boldsymbol{S}, G_\psi^*) \leq Q(\boldsymbol{X}; \boldsymbol{S}, G_\psi)$, $\forall \boldsymbol{X} \in \mathbb{C}^{M \times N}$, for any operator $G_\psi$ that makes $Q(\boldsymbol{X}; \boldsymbol{S}, G_\psi)$ a valid majorizer for $R_\psi$.

Under this criterion the operator $G_\psi^{\mathrm{R}}$ defined in (3.4) and (3.5) would be better than the operator $G_\psi^{\mathrm{L}}$ defined in (3.6); however, it is an open question if there is a better operator than $G_\psi^{\mathrm{R}}$. Answering this is important, as it would allow us to define better quadratic majorizers for the regularizer line search function and, therefore, it would improve our proposed majorize-minimize step-size selection strategy.

**Acknowledgments.** The authors thank Douglas Noll for discussions about MRI and Caroline Crockett for inspiration for some points.

## Appendix A. Proof of Theorem 2.4.

We first prove (i). Suppose $\psi$ is convex. Then for $\boldsymbol{x}, \boldsymbol{y} \in \mathbb{R}^r$ and $\alpha \in (0, 1)$:

$$\begin{aligned} f_\psi(\alpha \boldsymbol{x} + (1-\alpha)\boldsymbol{y}) &= \sum_{k=1}^{r} \psi(\alpha x_k + (1-\alpha)\, y_k) \\ &\leq \sum_{k=1}^{r} \alpha\, \psi(x_k) + (1-\alpha)\, \psi(y_k) = \alpha f_\psi(\boldsymbol{x}) + (1-\alpha) f_\psi(\boldsymbol{y}), \end{aligned}$$

using convexity of $\psi$ in the inequality. Thus $f_\psi$ is convex and hence $R_\psi$ is convex by Proposition 2.3 part (i) using the equivalent formulation for $R_\psi$ provided in (2.1).

Conversely, if $R_\psi$ is convex then Proposition 2.3 part (i) shows that $f_\psi$ is convex. Because $\psi(t) = \frac{1}{r} f_\psi(t\mathbf{1}_r)$ where $\mathbf{1}_r \in \mathbb{R}^r$ is the vector with each entry equal to one, it follows that for $\alpha \in (0, 1)$ and $t, s \in \mathbb{R}$:

$$\begin{aligned} \psi(\alpha t + (1-\alpha)\, s) &= \frac{1}{r} f_\psi(\alpha t \mathbf{1}_r + (1-\alpha) s \mathbf{1}_r) \\ &\leq \alpha \frac{1}{r} f_\psi(t\mathbf{1}_r) + (1-\alpha) \frac{1}{r} f_\psi(s\mathbf{1}_r) = \alpha\, \psi(t) + (1-\alpha)\, \psi(s), \end{aligned}$$

using convexity of $f_\psi$ in the inequality.

To prove (ii) we first calculate $\nabla f_\psi(\boldsymbol{\sigma}(\boldsymbol{X}))$. By definition of $f_\psi$, for any $\boldsymbol{x} \in \mathbb{R}^r$:

$$\nabla f_\psi(\boldsymbol{x}) = [\dot{\psi}(x_1), \ldots, \dot{\psi}(x_r)]^T = \dot{\psi}.(\boldsymbol{x}),$$

as $\psi$ is differentiable. Now we show that $f_\psi$ is locally Lipschitz, which follows from showing that $\nabla f_\psi$ is Lipschitz continuous. If $\boldsymbol{x}, \boldsymbol{y} \in \mathbb{R}^r$, then

$$\begin{aligned} \|\nabla f_\psi(\boldsymbol{x}) - \nabla f_\psi(\boldsymbol{y})\|^2 &= \sum_{k=1}^{r} |\, \dot{\psi}(x_k) - \dot{\psi}(y_k)\, |^2 \\ &\leq \sum_{k=1}^{r} \omega_\psi^2(0)\, |x_k - y_k|^2 = \omega_\psi^2(0)\, \|\boldsymbol{x} - \boldsymbol{y}\|^2, \end{aligned}$$

using the fact that $\dot{\psi}$ is $\omega_\psi(0)$-Lipschitz continuous (*cf.*, (2.5)) in the inequality. Therefore, $\nabla f_\psi$ is $\omega_\psi(0)$-Lipschitz continuous which implies that $f_\psi$ is locally Lipschitz. The result (2.9) follows from Proposition 2.3 part (ii) and (iii) using the equivalent formulation for $R_\psi$ provided in (2.1).

## Appendix B. Proof of Theorem 3.1.

It is clear from their definitions that $Q(\cdot\,;\boldsymbol{S},G_\psi^{\mathrm{R}})$ and $Q(\cdot\,;\boldsymbol{S},G_\psi^{\mathrm{L}})$ both satisfy the equality (3.1). Next, we prove that $Q(\cdot\,;\boldsymbol{S},G_\psi^{\mathrm{R}})$ satisfies (3.2), which is the main part of the proof. We then prove that $Q(\cdot\,;\boldsymbol{S},G_\psi^{\mathrm{L}})$ satisfies (3.2) by showing that $Q(\boldsymbol{X};\boldsymbol{S},G_\psi^{\mathrm{R}}) \leq Q(\boldsymbol{X};\boldsymbol{S},G_\psi^{\mathrm{L}})$, $\forall \boldsymbol{X} \in \mathbb{C}^{M\times N}$. Without loss of generality we assume that $M < N$ (wide case).

A key step in our proof uses the following inequality to lower bound the trace of a product of two Hermitian matrices [25, Thm. 4.3.53].

Proposition B.1 (Lower and upper bounds for the trace of the product of two Hermitian matrices). *Let $\boldsymbol{A} \in \mathbb{C}^{M\times M}$, $\boldsymbol{B} \in \mathbb{C}^{M\times M}$ be two Hermitian matrices with eigenvalues $\{\lambda_k(\boldsymbol{A})\}_{k=1}^M$ and $\{\lambda_k(\boldsymbol{B})\}_{k=1}^M$, respectively. Assuming both sets of eigenvalues are arranged in nonincreasing order,* i.e., *$\lambda_1(\boldsymbol{A}) \geq \lambda_2(\boldsymbol{A}) \geq \cdots \geq \lambda_M(\boldsymbol{A})$ and $\lambda_1(\boldsymbol{B}) \geq \lambda_2(\boldsymbol{B}) \geq \cdots \geq \lambda_M(\boldsymbol{B})$, it follows that:*

$$\sum_{k=1}^{M} \lambda_{M-k+1}(\boldsymbol{A})\,\lambda_k(\boldsymbol{B}) \leq \mathsf{trace}\{\boldsymbol{AB}\} \leq \sum_{k=1}^{M} \lambda_k(\boldsymbol{A})\,\lambda_k(\boldsymbol{B}). \tag{B.1}$$

Equipped with this inequality we now continue our proof. We start showing the inequality (3.2) when $\boldsymbol{S} \in \mathbb{C}^{M\times N}$ is a rectangular diagonal matrix of the form $\boldsymbol{S} = \mathsf{Diag}\{\boldsymbol{s}\}$, where $\boldsymbol{s} \in \mathbb{R}^M$ has nonnegative entries arranged in nonincreasing order (*i.e.*, $\boldsymbol{s} = \check{\boldsymbol{s}}$). We then generalize the result to generic rectangular matrices by leveraging the unitary invariance of $R_\psi$.

An important result used in our proof is given in the following lemma.

Lemma B.2. *Let $t, s, \in \mathbb{R}$. Then,*

$$\psi(s) - \psi(t) + \frac{1}{2}\,\omega_\psi(s)\,(t^2 - s^2) \geq 0. \tag{B.2}$$

*Proof.* Because $q_\psi$ is a majorizer for $\psi$:

$$\begin{aligned} 0 \leq q_\psi(t;s) - \psi(t) &= \psi(s) - \psi(t) + \dot{\psi}(s)(t-s) + \frac{1}{2}\,\omega_\psi(s)\,(t-s)^2 \\ &= \psi(s) - \psi(t) + s\,\omega_\psi(s)(t-s) + \frac{1}{2}\,\omega_\psi(s)\,(t^2 - 2ts + s^2) \\ &= \psi(s) - \psi(t) + \frac{1}{2}\,\omega_\psi(s)\,(t^2 - s^2). \end{aligned}$$

■

Next we extend Lemma B.2 to prove that $Q(\boldsymbol{X};\boldsymbol{S},G_\psi^{\mathrm{R}}) - R_\psi(\boldsymbol{X}) \geq 0$, $\forall \boldsymbol{X} \in \mathbb{C}^{M\times N}$ when $\boldsymbol{S} = \mathsf{Diag}\{\boldsymbol{s}\}$. In this case we have that $\boldsymbol{S} = \boldsymbol{U}\,\mathsf{Diag}\{\boldsymbol{\sigma}(\boldsymbol{S})\}\,\boldsymbol{V}'$ where $\boldsymbol{\sigma}(\boldsymbol{S}) = \boldsymbol{s}$, $\boldsymbol{U} = \boldsymbol{I}_M$, $\boldsymbol{V} = \boldsymbol{I}_N$, and $\boldsymbol{I}_K$ denotes the $K\times K$ identity matrix. This implies that $\nabla R_\psi(\boldsymbol{S}) = \mathsf{Diag}\Big\{\dot{\psi}.(\boldsymbol{s})\Big\}$

by Theorem 2.4. It follows that:

$$
\begin{aligned}
Q(\boldsymbol{X};\boldsymbol{S},G_\psi^{\mathrm{R}}) &= R_\psi(\mathsf{Diag}\{\boldsymbol{s}\}) + \mathrm{real}\Big\{\Big\langle \mathsf{Diag}\Big\{\dot\psi.(\boldsymbol{s})\Big\},\ \boldsymbol{X}-\mathsf{Diag}\{\boldsymbol{s}\}\Big\rangle\Big\} \\
&\quad + \frac{1}{2}(\mathbf{1}_M'(G_\psi^{\mathrm{R}}(\boldsymbol{s})\odot|\boldsymbol{X}-\mathsf{Diag}\{\boldsymbol{s}\}|.\hat{}\,2)\mathbf{1}_N) \qquad \text{(B.3)} \\
&= \sum_{k=1}^{M}\psi(s_k) + \mathrm{real}\Big\{\sum_{k=1}^{M}\dot\psi(s_k)\,(X_{kk}-s_k)\Big\} \qquad \text{(B.4)} \\
&\quad + \frac{1}{2}\sum_{k=1}^{M}\omega_\psi(s_k)\,|X_{kk}-s_k|^2 + \frac{1}{2}\sum_{k=1}^{M}\omega_\psi(s_k)\sum_{\substack{l=1\\l\neq k}}^{N}|X_{kl}|^2. \\
&= \sum_{k=1}^{M}\psi(s_k) + s_k\,\omega_\psi(s_k)\,(\mathrm{real}\{X_{kk}\}-s_k) \\
&\quad + \frac{1}{2}\,\omega_\psi(s_k)(|X_{kk}|^2 - 2s_k\,\mathrm{real}\{X_{kk}\}+s_k^2) + \frac{1}{2}\sum_{\substack{l=1\\l\neq k}}^{N}\omega_\psi(s_k)\,|X_{kl}|^2 \\
&= \sum_{k=1}^{M}\psi(s_k) + \frac{1}{2}\,\omega_\psi(s_k)(|X_{kk}|^2 - s_k^2) + \frac{1}{2}\sum_{\substack{l=1\\l\neq k}}^{N}\omega_\psi(s_k)\,|X_{kl}|^2 \\
&= \left(\sum_{k=1}^{M}\psi(s_k) - \frac{1}{2}\,\omega_\psi(s_k)\,s_k^2\right) + \frac{1}{2}\sum_{k=1}^{M}\omega_\psi(s_k)\sum_{l=1}^{N}|X_{kl}|^2. \qquad \text{(B.5)}
\end{aligned}
$$

The next step is to derive a lower bound for the last sum of the previous equation in terms of the singular values of $\boldsymbol{X}$. For this we first write this term as the trace of the product of two Hermitian matrices and use (B.1) as follows:

$$
\begin{aligned}
\sum_{k=1}^{M}\omega_\psi(s_k)\sum_{l=1}^{N}|X_{kl}|^2 &= \mathsf{trace}\left\{\left(\mathsf{Diag}\left\{\sqrt{\omega_\psi.(\boldsymbol{s})}\right\}\right)'\boldsymbol{X}\left(\left(\mathsf{Diag}\left\{\sqrt{\omega_\psi.(\boldsymbol{s})}\right\}\right)'\boldsymbol{X}\right)'\right\} \\
&= \mathsf{trace}\left\{\underbrace{\mathsf{Diag}\left\{\sqrt{\omega_\psi.(\boldsymbol{s})}\right\}\left(\mathsf{Diag}\left\{\sqrt{\omega_\psi.(\boldsymbol{s})}\right\}\right)'}_{\boldsymbol{A}\in\mathbb{C}^{M\times M}}\underbrace{\boldsymbol{X}\boldsymbol{X}'}_{\boldsymbol{B}\in\mathbb{C}^{M\times M}}\right\} \\
&= \mathsf{trace}\{\boldsymbol{A}\boldsymbol{B}\} \geq \sum_{k=1}^{M}\lambda_{M-k+1}(\boldsymbol{A})\lambda_k(\boldsymbol{B}).
\end{aligned}
$$

We have that $\lambda_{M-k+1}(\boldsymbol{A}) = \omega_\psi(s_k)$ given that $\omega_\psi$ is monotone nonincreasing, and that $\lambda_k(\boldsymbol{B}) = \sigma_k^2(\boldsymbol{X})$. It follows that:

$$
\sum_{k=1}^{M}\omega_\psi(s_k)\sum_{l=1}^{N}|X_{kl}|^2 \geq \sum_{k=1}^{M}\omega_\psi(s_k)\,\sigma_k^2(\boldsymbol{X}). \qquad \text{(B.6)}
$$

Using this inequality to lower bound the right-hand-side in (B.5), Lemma B.2 shows that:

$$Q(\boldsymbol{X};\boldsymbol{S},G_\psi^{\mathrm{R}}) - R_\psi(\boldsymbol{X}) \geq \sum_{k=1}^{M} \psi(s_k) - \psi(\sigma_k(\boldsymbol{X})) + \frac{1}{2}\,\omega_\psi(s_k)(\sigma_k^2(\boldsymbol{X}) - s_k^2) \geq 0. \tag{B.7}$$

Now we prove the general case. Let $\boldsymbol{Y},\boldsymbol{S} \in \mathbb{C}^{M\times N}$ and $\boldsymbol{U} \in \mathbb{C}^{M\times M}, \boldsymbol{V} \in \mathbb{C}^{N\times N}$ denote two unitary matrices such that $\boldsymbol{S} = \boldsymbol{U}\,\mathsf{Diag}\{\boldsymbol{\sigma}(\boldsymbol{S})\}\,\boldsymbol{V}'$. Because $R_\psi$ is unitarily invariant, it follows that:

$$\begin{aligned}
R_\psi(\boldsymbol{Y}+\boldsymbol{S}) &= R_\psi(\boldsymbol{U}'(\boldsymbol{Y}+\boldsymbol{S})\boldsymbol{V}) = R_\psi(\boldsymbol{U}'\boldsymbol{Y}\boldsymbol{V} + \mathsf{Diag}\{\boldsymbol{\sigma}(\boldsymbol{S})\}) \\
&\leq Q(\boldsymbol{U}'\boldsymbol{Y}\boldsymbol{V} + \mathsf{Diag}\{\boldsymbol{\sigma}(\boldsymbol{S})\}; \mathsf{Diag}\{\boldsymbol{\sigma}(\boldsymbol{S})\}, G_\psi^{\mathrm{R}}) \quad \text{by (B.7)} \\
&= R_\psi(\mathsf{Diag}\{\boldsymbol{\sigma}(\boldsymbol{S})\}) + \mathrm{real}\big\{\langle \nabla R_\psi(\mathsf{Diag}\{\boldsymbol{\sigma}(\boldsymbol{S})\}),\, \boldsymbol{U}'\boldsymbol{Y}\boldsymbol{V}\rangle\big\} \\
&\quad + \frac{1}{2}(\mathbf{1}_M'(G_\psi^{\mathrm{R}}(\boldsymbol{\sigma}(\boldsymbol{S})) \odot |\boldsymbol{U}'\boldsymbol{Y}\boldsymbol{V}|.\hat{}\,2)\mathbf{1}_N) \quad \text{by (3.3)} \\
&= R_\psi(\boldsymbol{S}) + \mathrm{real}\Big\{\Big\langle \mathsf{Diag}\Big\{\dot{\psi}.(\boldsymbol{\sigma}(\boldsymbol{S}))\Big\},\, \boldsymbol{U}'\boldsymbol{Y}\boldsymbol{V}\Big\rangle\Big\} \quad \text{by (2.9)} \\
&\quad + \frac{1}{2}(\mathbf{1}_M'(G_\psi^{\mathrm{R}}(\boldsymbol{\sigma}(\boldsymbol{S})) \odot |\boldsymbol{U}'\boldsymbol{Y}\boldsymbol{V}|.\hat{}\,2)\mathbf{1}_N) \\
&= R_\psi(\boldsymbol{S}) + \mathrm{real}\Big\{\mathsf{trace}\Big\{\mathsf{Diag}\Big\{\dot{\psi}.(\boldsymbol{\sigma}(\boldsymbol{S}))\Big\}\,\boldsymbol{V}'\boldsymbol{Y}'\boldsymbol{U}\Big\}\Big\} \\
&\quad + \frac{1}{2}(\mathbf{1}_M'(G_\psi^{\mathrm{R}}(\boldsymbol{\sigma}(\boldsymbol{S})) \odot |\boldsymbol{U}'\boldsymbol{Y}\boldsymbol{V}|.\hat{}\,2)\mathbf{1}_N) \\
&= R_\psi(\boldsymbol{S}) + \mathrm{real}\Big\{\mathsf{trace}\Big\{\boldsymbol{U}\,\mathsf{Diag}\Big\{\dot{\psi}.(\boldsymbol{\sigma}(\boldsymbol{S}))\Big\}\,\boldsymbol{V}'\boldsymbol{Y}'\Big\}\Big\} \\
&\quad + \frac{1}{2}(\mathbf{1}_M'(G_\psi^{\mathrm{R}}(\boldsymbol{\sigma}(\boldsymbol{S})) \odot |\boldsymbol{U}'\boldsymbol{Y}\boldsymbol{V}|.\hat{}\,2)\mathbf{1}_N) \\
&= R_\psi(\boldsymbol{S}) + \mathrm{real}\{\langle \nabla R_\psi(\boldsymbol{S}),\, \boldsymbol{Y}\rangle\} + \frac{1}{2}(\mathbf{1}_M'(G_\psi^{\mathrm{R}}(\boldsymbol{\sigma}(\boldsymbol{S})) \odot |\boldsymbol{U}'\boldsymbol{Y}\boldsymbol{V}|.\hat{}\,2)\mathbf{1}_N), \qquad \text{(B.8)}
\end{aligned}$$

using the cyclic property of the trace in the next to last equality. The result follows from setting $\boldsymbol{Y}$ to $\boldsymbol{X}-\boldsymbol{S}$ in (B.8).

To show that $Q(\boldsymbol{X};\boldsymbol{S},G_\psi^{\mathrm{R}}) \leq Q(\boldsymbol{X};\boldsymbol{S},G_\psi^{\mathrm{L}})$, $\forall \boldsymbol{X} \in \mathbb{C}^{M\times N}$, it is enough to show that $\mathbf{1}_M'(G_\psi^{\mathrm{R}}(\boldsymbol{\sigma}(\boldsymbol{S})) \odot |\boldsymbol{U}'(\boldsymbol{X}-\boldsymbol{S})\boldsymbol{V}|.\hat{}\,2)\mathbf{1}_N \leq \mathbf{1}_M'(G_\psi^{\mathrm{L}}(\boldsymbol{\sigma}(\boldsymbol{S})) \odot |\boldsymbol{U}'(\boldsymbol{X}-\boldsymbol{S})\boldsymbol{V}|.\hat{}\,2)\mathbf{1}_N$, which is equivalent to showing that:

$$\begin{aligned}
\sum_{k=1}^{M} \omega_\psi(\sigma_k(\boldsymbol{S})) \sum_{l=1}^{N} |[\boldsymbol{U}'(\boldsymbol{X}-\boldsymbol{S})\boldsymbol{V}]_{kl}|^2 &\leq \sum_{k=1}^{M} \Big(\sup_{t\in\mathbb{R}} \omega_\psi(t)\Big) \sum_{l=1}^{N} |[\boldsymbol{U}'(\boldsymbol{X}-\boldsymbol{S})\boldsymbol{V}]_{kl}|^2 \\
&= \sum_{k=1}^{M}\sum_{l=1}^{N} \omega_\psi(0)\,|[\boldsymbol{U}'(\boldsymbol{X}-\boldsymbol{S})\boldsymbol{V}]_{kl}|^2,
\end{aligned}$$

where we have used the property that $\sup_{t\in\mathbb{R}} \omega_\psi(t) = \omega_\psi(0)$ as $\psi$ is even and $\omega_\psi(t)$ is monotonic nonincreasing for $t > 0$.

The proof for the tall case, *i.e.*, when $M > N$, is analogous and is omitted for the sake of space. Finally we prove (3.7), (3.11), and (3.9). To prove (3.7) it is enough to show that:

$$\big\|\boldsymbol{W}_{\psi,\boldsymbol{S}}'(\boldsymbol{X}-\boldsymbol{S})\big\|_{\mathrm{F}}^2 = \mathbf{1}_M'(G_\psi^{\mathrm{R}}(\boldsymbol{\sigma}(\boldsymbol{S})) \odot |\boldsymbol{U}'(\boldsymbol{X}-\boldsymbol{S})\boldsymbol{V}|.\hat{}\,2)\mathbf{1}_N.$$

Because the Frobenius norm is unitarily invariant we have that:

$$\begin{aligned}\left\|\boldsymbol{W}'_{\psi,\boldsymbol{S}}(\boldsymbol{X}-\boldsymbol{S})\right\|_{\mathrm{F}}^2 &= \left\|\boldsymbol{V}'\left(\mathsf{Diag}\left\{\sqrt{\omega_\psi.(\boldsymbol{\sigma}(\boldsymbol{s}))}\right\}\right)'\boldsymbol{U}'(\boldsymbol{X}-\boldsymbol{S})\right\|_{\mathrm{F}}^2\\ &= \left\|\left(\mathsf{Diag}\left\{\sqrt{\omega_\psi.(\boldsymbol{\sigma}(\boldsymbol{s}))}\right\}\right)'\boldsymbol{U}'(\boldsymbol{X}-\boldsymbol{S})\boldsymbol{V}\right\|_{\mathrm{F}}^2\\ &= \sum_{k=1}^{M}\omega_\psi(\sigma_k(\boldsymbol{S}))\sum_{l=1}^{N}|[\boldsymbol{U}'(\boldsymbol{X}-\boldsymbol{S})\boldsymbol{V}]_{kl}|^2\\ &= \mathbf{1}'_M(G_\psi^{\mathrm{R}}(\boldsymbol{\sigma}(\boldsymbol{S})\odot|\boldsymbol{U}'(\boldsymbol{X}-\boldsymbol{S})\boldsymbol{V}|.\hat{}2)\mathbf{1}_N.\end{aligned}$$

The proofs for (3.9) and (3.11) are analogous to the previous proof and are omitted.

**Appendix C. Proof of proposition 2.6.** Let $\boldsymbol{X},\boldsymbol{S}\in\mathbb{C}^{M\times N}$, and $\boldsymbol{U},\boldsymbol{V}$ denote suitable sized unitary matrices such that $\boldsymbol{S}=\boldsymbol{U}\,\mathsf{Diag}\{\boldsymbol{\sigma}(\boldsymbol{S})\}\,\boldsymbol{V}'$. Using (3.11) in Theorem 3.1:

$$R_\psi(\boldsymbol{X})\le R_\psi(\boldsymbol{S})+\mathrm{real}\{\langle\nabla R_\psi(\boldsymbol{S}),\,\boldsymbol{X}-\boldsymbol{S}\rangle\}+\frac{1}{2}\,\omega_\psi(0)\,\|\boldsymbol{X}-\boldsymbol{S}\|_{\mathrm{F}}^2\,, \tag{C.1}$$

which is equivalent to $\nabla R_\psi$ being $\omega_\psi(0)$-Lipschitz [2, Thm. 5.8] for the inner product in (2.7).

**Appendix D. Proof of Theorem 3.2.** We need to verify that

$$h_\psi(\bar\alpha;\boldsymbol{X},\boldsymbol{\Delta}) = g_{h_\psi}(\bar\alpha;\bar\alpha,\boldsymbol{X},\boldsymbol{\Delta},G_\psi), \tag{D.1}$$

$$h_\psi(\alpha;\boldsymbol{X},\boldsymbol{\Delta}) \le g_{h_\psi}(\alpha;\bar\alpha,\boldsymbol{X},\boldsymbol{\Delta},G_\psi),\quad \forall\alpha\in\mathbb{R}. \tag{D.2}$$

(D.1) is easy to verify from the definition of $g_{h_\psi}(\cdot\,;\bar\alpha,\boldsymbol{X},\boldsymbol{\Delta},G_\psi)$. To prove (D.2) we use the fact that $Q(\cdot\,;\boldsymbol{X}+\bar\alpha\boldsymbol{\Delta},G_\psi)$ is a majorizer for $R_\psi$ at $\boldsymbol{X}+\bar\alpha\boldsymbol{\Delta}$. We have that:

$$\begin{aligned}h_\psi(\alpha;\boldsymbol{X},\boldsymbol{\Delta}) &= R_\psi(\boldsymbol{X}+\alpha\boldsymbol{\Delta})\\ &\le Q(\boldsymbol{X}+\alpha\boldsymbol{\Delta}\,;\boldsymbol{X}+\bar\alpha\boldsymbol{\Delta},G_\psi)\\ &= R_\psi(\boldsymbol{X}+\bar\alpha\boldsymbol{\Delta})+\mathrm{real}\{\langle\nabla R_\psi(\boldsymbol{X}+\bar\alpha\boldsymbol{\Delta}),\,\boldsymbol{X}+\alpha\boldsymbol{\Delta}-(\boldsymbol{X}+\bar\alpha\boldsymbol{\Delta})\rangle\}\\ &\quad+\frac{1}{2}\mathbf{1}'_M(G_\psi(\boldsymbol{\sigma}(\boldsymbol{X}+\bar\alpha\boldsymbol{\Delta}))\odot(\boldsymbol{U}'(\boldsymbol{X}+\alpha\boldsymbol{\Delta}-(\boldsymbol{X}+\bar\alpha\boldsymbol{\Delta}))\boldsymbol{V}).\hat{}2)\mathbf{1}_N\\ &= R_\psi(\boldsymbol{X}+\bar\alpha\boldsymbol{\Delta})+\mathrm{real}\{\langle\nabla R_\psi(\boldsymbol{X}+\bar\alpha\boldsymbol{\Delta}),\,\boldsymbol{\Delta}\rangle\}(\alpha-\bar\alpha)\\ &\quad+\frac{1}{2}\mathbf{1}'_M(G_\psi(\boldsymbol{\sigma}(\boldsymbol{X}+\bar\alpha\boldsymbol{\Delta}))\odot(\boldsymbol{U}'\boldsymbol{\Delta}\boldsymbol{V}).\hat{}2)\mathbf{1}_N(\alpha-\bar\alpha)^2.\\ &= g_{h_\psi}(\alpha;\bar\alpha,\boldsymbol{X},\boldsymbol{\Delta},G_\psi),\quad\forall\alpha,\bar\alpha\in\mathbb{R}.\end{aligned}$$

**Appendix E. Proof of Corollary 3.3.** Without loss of generality we assume that $M<N$ (wide case). The first part of the corollary follows directly from Theorem 3.1 and Theorem 3.2. To show the second part it is enough to show that $\mathbf{1}'_M(G_\psi^{\mathrm{R}}(\boldsymbol{\sigma}(\boldsymbol{X}+\bar\alpha\boldsymbol{\Delta}))\odot|\boldsymbol{U}'\boldsymbol{\Delta}\boldsymbol{V}|.\hat{}2)\mathbf{1}_N\le$

$\mathbf{1}'_M(G^{\mathrm{L}}_\psi(\boldsymbol{\sigma}(\boldsymbol{X}+\bar{\alpha}\boldsymbol{\Delta}))\odot|\boldsymbol{U}'\boldsymbol{\Delta}\boldsymbol{V}|.\hat{}2)\mathbf{1}_N$. This is equivalent to showing that:

$$\sum_{k=1}^{M}\omega_\psi(\sigma_k(\boldsymbol{X}+\bar{\alpha}\boldsymbol{\Delta}))\sum_{l=1}^{N}|[\boldsymbol{U}'\boldsymbol{\Delta}\boldsymbol{V}]_{kl}|^2\le\left(\sup_{t\in\mathbb{R}}\omega_\psi(t)\right)\sum_{k=1}^{M}\sum_{l=1}^{N}|[\boldsymbol{U}'\boldsymbol{\Delta}\boldsymbol{V}]_{kl}|^2$$
$$=\omega_\psi(0)\sum_{k=1}^{M}\sum_{l=1}^{N}|[\boldsymbol{U}'\boldsymbol{\Delta}\boldsymbol{V}]_{kl}|^2.$$

**Appendix F. Proof of Proposition 4.1.** We first prove the sufficient condition by providing an equivalent expression for $f_{\psi,\boldsymbol{w}}$ in (4.2) inspired by the c-spectral norm in [34]. For this purpose we review *generalized permutation matrices.*

Definition F.1 (Generalized permutation matrix [34]). *A $r\times r$ matrix $\boldsymbol{P}$ is a generalized permutation matrix if it has exactly one nonzero entry in each row and each column, that entry being equal to 1 or $-1$. We denote the set of $r\times r$ generalized permutation matrices by $\Theta_r$.*

Using the previous definition we first show that:

$$f_{\psi,\boldsymbol{w}}(\boldsymbol{x})=\max_{\boldsymbol{P}\in\Theta_r}\langle\boldsymbol{w},\,\psi.(\boldsymbol{P}\boldsymbol{x})\rangle, \tag{F.1}$$

where here $\langle\cdot,\,\cdot\rangle$ denotes the Euclidean inner product in $\mathbb{R}^r$. Given that $\check{\boldsymbol{x}}$ is constructed by sorting the entries of $|\boldsymbol{x}|$, there exists $\check{\boldsymbol{P}}\in\Theta_r$ such that $\check{\boldsymbol{x}}=\check{\boldsymbol{P}}\boldsymbol{x}$. Then, from (4.2):

$$f_{\psi,\boldsymbol{w}}(\boldsymbol{x})=\sum\nolimits_{k=1}^{r}w_k\,\psi\big([\check{\boldsymbol{P}}\boldsymbol{x}]_k\big)=\langle\boldsymbol{w},\,\psi.(\check{\boldsymbol{P}}\boldsymbol{x})\rangle\le\max_{\boldsymbol{P}\in\Theta_r}\langle\boldsymbol{w},\,\psi.(\boldsymbol{P}\boldsymbol{x})\rangle\,.$$

We prove the reverse inequality by contradiction. If the inequality is not true, then there is an $\boldsymbol{x}$ and a generalized permutation matrix $\boldsymbol{P}^*\in\Theta_r$ such that $\boldsymbol{P}^*\boldsymbol{x}\neq\check{\boldsymbol{x}}$ and

$$0\le f_{\psi,\boldsymbol{w}}(\boldsymbol{x})<\langle\boldsymbol{w},\,\psi.(\boldsymbol{P}^*\boldsymbol{x})\rangle=\sum\nolimits_{k=1}^{r}w_k\,\psi([\boldsymbol{P}^*\boldsymbol{x}]_k)\,.$$

Because $\boldsymbol{P}^*\boldsymbol{x}\neq\check{\boldsymbol{x}}$, there are entries $k_1,k_2\in\{1,\dots,r\}$ where $k_1<k_2$, such that $|[\boldsymbol{P}^*\boldsymbol{x}]_{k_1}|<|[\boldsymbol{P}^*\boldsymbol{x}]_{k_2}|$. Because the weights are nonincreasing, and $\psi(t)$ is even and nondecreasing for $t>0$, it follows that

$$w_{k_1}\,\psi(|[\boldsymbol{P}^*\boldsymbol{x}]_{k_2}|)\ge w_{k_2}\,\psi(|[\boldsymbol{P}^*\boldsymbol{x}]_{k_1}|)\,.$$

Let $\boldsymbol{P}_{k_1,k_2}$ denote the generalized permutation matrix that swaps the $k_1$th and $k_2$th entries and multiplies each entry either by 1 or -1 to make both entries nonnegative. Then we have that

$$\langle\boldsymbol{w},\,\psi.(\boldsymbol{P}^*\boldsymbol{x})\rangle=\sum_{k=1}^{r}w_k\,\psi([\boldsymbol{P}^*\boldsymbol{x}]_k)\le\sum_{k=1}^{r}w_k\,\psi([\boldsymbol{P}_{k_1,k_2}\boldsymbol{P}^*\boldsymbol{x}]_k)=\langle\boldsymbol{w},\,\psi.(\boldsymbol{P}_{k_1,k_2}\boldsymbol{P}^*\boldsymbol{x})\rangle\,.$$

At this point either $\boldsymbol{P}_{k_1,k_2}\boldsymbol{P}^*\boldsymbol{x}=\check{\boldsymbol{x}}$ or we can find another pair of entries in $\boldsymbol{P}_{k_1,k_2}\boldsymbol{P}^*\boldsymbol{x}$ that can be swapped and made nonnegative to majorize $\langle\boldsymbol{w},\,\psi.(\boldsymbol{P}_{k_1,k_2}\boldsymbol{P}^*\boldsymbol{x})\rangle$. Continuing this process we finally obtain that $f_{\psi,\boldsymbol{w}}(\boldsymbol{x})<\langle\boldsymbol{w},\,\psi.(\boldsymbol{P}^*\boldsymbol{x})\rangle\le f_{\psi,\boldsymbol{w}}(\boldsymbol{x})$, which is a contradiction. Therefore,

$$f_{\psi,\boldsymbol{w}}(\boldsymbol{x})\ge\max_{\boldsymbol{P}\in\Theta_r}\langle\boldsymbol{w},\,\psi.(\boldsymbol{P}\boldsymbol{x})\rangle\,.$$

It is easy to show that each function $\gamma_\psi(\boldsymbol{x}; \boldsymbol{w}, \boldsymbol{P}) \triangleq \langle \boldsymbol{w},\, \psi\,.(\boldsymbol{P}\boldsymbol{x})\rangle,\ \boldsymbol{P} \in \Theta_r$ is convex when $\psi$ is convex. Then, $f_{\psi,\boldsymbol{w}}$ is convex as it can be written as the pointwise supremum of a collection of convex functions [55, Thm. 5.5].

We now prove the necessary conditions. Noting that $\psi(t) = f_{\psi,\boldsymbol{w}}(\boldsymbol{1}_r t)/\sum_{k=1}^r w_k$, convexity of $\psi$ follows from convexity of $f_{\psi,\boldsymbol{w}}$ because convexity is preserved under affine maps and nonnegative scaling.

Now we show that the entries of $\boldsymbol{w}$ must be nonincreasing, using proof by contradiction.

Consider first the case where $r = 2$ with $0 \le w_1 < w_2$ and define $\boldsymbol{x} = \begin{bmatrix} u \\ v \end{bmatrix}$ and $\boldsymbol{y} = \begin{bmatrix} v \\ u \end{bmatrix}$ for $0 < u < v < \epsilon\, u$, where $\epsilon > 1$. In addition, we pick $u$ and $v$ such that $\omega_\psi(\alpha v + (1-\alpha)\, u) > 0,\ \forall \alpha \in (0,1)$. This is possible as $\omega_\psi$ is not always equal to 0 unless $\psi$ is a constant, which is precluded by our ongoing assumptions. Define

$$\begin{aligned} g(\alpha) \triangleq f_{\psi,\boldsymbol{w}}(\alpha\boldsymbol{x} + (1-\alpha)\boldsymbol{y}) &= f_{\psi,\boldsymbol{w}}\left(\begin{bmatrix} \alpha u + (1-\alpha)v \\ \alpha v + (1-\alpha)u \end{bmatrix}\right) \\ &= \begin{cases} w_1\, \psi(\alpha u + (1-\alpha)\, v) + w_2\, \psi(\alpha v + (1-\alpha)\, u), & 0 \le \alpha \le 1/2 \\ w_1\, \psi(\alpha v + (1-\alpha)\, u) + w_2\, \psi(\alpha u + (1-\alpha)\, v), & 1/2 \le \alpha \le 1. \end{cases} \end{aligned}$$

We will show that $g$ is nonconvex, which means that $f_{\psi,\boldsymbol{w}}$ must be nonconvex, by showing that $g$ increases on $(0, 1/2)$ and then decreases on $(1/2, 1)$.

If $\alpha \in (0, \frac{1}{2})$, then $\dot{g}(\alpha)$, *i.e.*, the derivative of $g$ with respect to $\alpha$, satisfies:

$$\begin{aligned} \dot{g}(\alpha) &= w_1\, \dot{\psi}(\alpha u + (1-\alpha)\, v)\, (u - v) + w_2\, \dot{\psi}(\alpha v + (1-\alpha)\, u)\, (v - u) \\ &= (v-u)\, \big(w_2\ \dot{\psi}(\alpha v + (1-\alpha)\, u) - w_1\ \dot{\psi}(\alpha u + (1-\alpha)\, v)\big) \\ &= (v-u)\, \big(w_2\, (\alpha v + (1-\alpha)u)\ \omega_\psi(\alpha v + (1-\alpha)\, u) \\ &\qquad - w_1\, (\alpha u + (1-\alpha)v)\ \omega_\psi(\alpha u + (1-\alpha)\, v)\big), \end{aligned}$$

where we used that $\dot{\psi}(t) = t\, \omega_\psi(t)$ in the last equality. Next, because $\omega_\psi(t)$ is monotonic nonincreasing for $t > 0$:

$$\omega_\psi(\alpha v + (1-\alpha)\, u) \ge \omega_\psi(\alpha u + (1-\alpha)\, v).$$

Using this in the previous equation implies that:

$$\begin{aligned} \dot{g}(\alpha) &\ge C\, \big(w_2\, (\alpha v + (1-\alpha)u) - w_1\, (\alpha u + (1-\alpha)v) \\ &= C\, \big(u\, (w_2 - \alpha\, (w_2 + w_1)) - v\, (w_1 - \alpha\, (w_2 + w_1))\big), \end{aligned}$$

where $C \triangleq (v-u)\, \omega_\psi(\alpha v + (1-\alpha)\, u) > 0$. Because $\alpha < 1/2$, the term multiplying $v$ is positive. Using $v < \epsilon\, u$ in the previous inequality yields:

$$\begin{aligned} \dot{g}(\alpha) &> C\, \big(u\, (w_2 - \alpha\, (w_2 + w_1)) - \epsilon\, u\, (w_1 - \alpha\, (w_2 + w_1))\big) \\ &= C\, u\, \big(w_2\, (1 + \alpha(\epsilon - 1)) - w_1\, (\alpha + \epsilon(1-\alpha))\big). \end{aligned}$$

If $w_1 = 0$ then we have that $\dot{g}(\alpha) > 0$ and we can conclude that $g$ is increasing for $\alpha \in (0, \frac{1}{2})$. If $w_1 > 0$ then we can choose $\epsilon = \frac{w_2}{w_1}$ to simplify the lower bound and obtain that

$$\dot{g}(\alpha) > C\, u\, \alpha\, (w_2^2 - w_1^2)/w_1 > 0. \quad \text{(given that } w_2 > w_1)$$

Therefore, $g$ is increasing for $\alpha \in (0, \frac{1}{2})$. Proceeding analogously for the case $\alpha \in (\frac{1}{2}, 1)$ we obtain the upper bound

$$\dot{g}(\alpha) < D\,u\,(1-\alpha)(w_1^2 - w_2^2)/w_1 < 0, \quad \text{(given that } w_2 > w_1\text{)}$$

where $D \triangleq (v-u)\,\omega_\psi(\alpha u + (1-\alpha)\,v) > 0$. Thus, $g$ is decreasing for $\alpha \in (\frac{1}{2}, 1)$. We omit some of the algebraic derivations for this case, as they are analogous to the ones in the first case. Therefore, $g$ is nonconvex as it is increasing before $\alpha = \frac{1}{2}$ and decreasing after $\alpha = \frac{1}{2}$. This implies that $f_{\psi,\boldsymbol{w}}$ is nonconvex which is a contradiction. This concludes the proof for the case $r = 2$.

We now prove the general case $r > 2$ also by contradiction. Suppose there is $K \in \{1, \ldots, r-1\}$ such that $w_K < w_{K+1}$, and pick $\boldsymbol{x} \in \mathbb{R}^r$ such that $0 < x_1 < x_2 < \ldots < x_r$. Let $\boldsymbol{y} \in \mathbb{R}^r$ have entries that are the same entries as $\boldsymbol{x}$ except that the $(r-K)$th and $(r-K+1)$th entries are swapped, *i.e.*, $y_{r-K+1} = x_{r-K}$ and $y_{r-K} = x_{r-K+1}$. We choose $x_{r-K+1} < \epsilon\, x_{r-K}$ for some $\epsilon > 1$. Under this setting we have that

$$g(\alpha) = w_K\,\psi(M_\alpha) + w_{K+1}\,\psi(m_\alpha) + \sum_{\substack{k=1 \\ k \notin \{K, K+1\}}}^{r} w_k\,\psi(x_{r-k+1}),$$

where

$$M_\alpha \triangleq \max(\alpha x_{r-K} + (1-\alpha)x_{r-K+1}\ ,\ \alpha x_{r-K+1} + (1-\alpha)x_{r-K}),$$
$$m_\alpha \triangleq \min(\alpha x_{r-K} + (1-\alpha)x_{r-K+1}\ ,\ \alpha x_{r-K+1} + (1-\alpha)x_{r-K}),$$

which implies that

$$\dot{g}(\alpha) = w_K M_\alpha\,\dot{\psi}(M_\alpha) + w_{K+1} m_\alpha\,\dot{\psi}(m_\alpha),$$

which can be analyzed following the same procedure shown for the case $r = 2$. Therefore, $g$ is nonconvex which implies that $f_{\psi,\boldsymbol{w}}$ is nonconvex, which is a contradiction. This concludes our proof.

## Appendix G. Proof of Proposition 4.2.

Let $0 < \delta < \min_{k \in \{1,\ldots,r\}} |x_k - x_{k-1}|$, where we have defined $x_0 = 0$. Then any vector within the ball with center at $\boldsymbol{x}$ and radius $\delta$ has entries that are nonnegative, nonrepeated, and arranged in decreasing order. More formally,

$$\boldsymbol{y} \in B_\delta(\boldsymbol{x}) \iff \boldsymbol{y} = \check{\boldsymbol{y}}, \tag{G.1}$$

where $B_\delta(\boldsymbol{x}) \triangleq \{\boldsymbol{y} \in \mathbb{R}^r \mid \|\boldsymbol{x} - \boldsymbol{y}\| \leq \delta\}$, with $\|\cdot\|$ denoting the Euclidean norm. It follows that:

$$f_{\psi,\boldsymbol{w}}(\boldsymbol{y}) = \sum_{k=1}^{r} w_k\,\psi([\check{\boldsymbol{y}}]_k) = \sum_{k=1}^{r} w_k\,\psi([\boldsymbol{y}]_k) = \langle \boldsymbol{w},\, \psi.(\boldsymbol{y})\rangle,\ \forall \boldsymbol{y} \in B_\delta(\boldsymbol{x}). \tag{G.2}$$

The result follows from showing that $\langle \boldsymbol{w},\, \psi.(\boldsymbol{y})\rangle$ is locally Lipschitz when $\boldsymbol{y} \in B_\delta(\boldsymbol{x})$, and differentiable at $\boldsymbol{x}$ with gradient given by $\boldsymbol{w} \odot \dot{\psi}.(\boldsymbol{x})$. Showing the differentiability and gradient

formula for $\langle \boldsymbol{w},\, \psi.(\boldsymbol{y})\rangle$ is straightfoward and follows from the differentiability of $\psi$. We now show that the gradient of $f_{\psi,\boldsymbol{w}}$ is Lipschitz continuous, which implies that $f_{\psi,\boldsymbol{w}}$ is locally Lipschitz at $\boldsymbol{x}$. Let $\boldsymbol{u}, \boldsymbol{v} \in B_\delta(\boldsymbol{x})$, then

$$\begin{aligned}\left\| \boldsymbol{w} \odot \dot{\psi}.(\boldsymbol{u}) - \boldsymbol{w} \odot \dot{\psi}.(\boldsymbol{v}) \right\|^2 &= \sum_{k=1}^{r} w_k^2 \,|\, \dot{\psi}(u_k) - \dot{\psi}(v_k) \,|^2 \\ &\leq \|\boldsymbol{w}\|_\infty^2 \sum_{k=1}^{r} |\, \dot{\psi}(u_k) - \dot{\psi}(v_k) \,|^2 \\ &\leq \|\boldsymbol{w}\|_\infty^2 \, \omega_\psi^2(0) \, \|\boldsymbol{u} - \boldsymbol{v}\|^2 \end{aligned} \tag{G.3}$$

as $\dot{\psi}$ is $\omega_\psi(0)$-Lipschitz continuous. Therefore, the gradient of $\langle \boldsymbol{w},\, \psi.(\boldsymbol{y})\rangle$ is $L$-Lipschitz continuous with $L = \|\boldsymbol{w}\|_\infty \, \omega_\psi(0)$.

## Appendix H. Majorizers for weighted Huber-based low-rank regularizers.

A majorizer $Q_{\boldsymbol{w}}(\cdot\,; \boldsymbol{S}, G_{\psi,\boldsymbol{w}})$ as defined in (4.5) should satisfy:

$$R_{\psi,\boldsymbol{w}}(\boldsymbol{S}) = Q_{\boldsymbol{w}}(\boldsymbol{S}; \boldsymbol{S}, G_{\psi,\boldsymbol{w}}), \tag{H.1}$$

$$R_{\psi,\boldsymbol{w}}(\boldsymbol{X}) \leq Q_{\boldsymbol{w}}(\boldsymbol{X}; \boldsymbol{S}, G_{\psi,\boldsymbol{w}}), \quad \forall \boldsymbol{X} \in \mathbb{C}^{M\times N}. \tag{H.2}$$

Particularly, we show that two operators, denoted by $G^{\mathrm{R}}_{\psi,\boldsymbol{w}}$ and $G^{\mathrm{L}}_{\psi,\boldsymbol{w}}$, when used in (4.5), lead to valid majorizers for $R_{\psi,\boldsymbol{w}}$, *i.e.*, in both cases the resulting $Q_{\boldsymbol{w}}$ satisfies (H.1) and (H.2), when $\boldsymbol{w}$ has nondecreasing entries. When $M < N$ (wide case), we define $G^{\mathrm{R}}_{\psi,\boldsymbol{w}}$ and $G^{\mathrm{L}}_{\psi,\boldsymbol{w}}$ as the following generalizations of (3.4)–(3.6):

$$G^{\mathrm{R}}_{\psi,\boldsymbol{w}}(\boldsymbol{s}) \triangleq (\boldsymbol{w} \odot \omega_\psi.(\boldsymbol{s}))\mathbf{1}'_N, \tag{H.3}$$

$$G^{\mathrm{L}}_{\psi,\boldsymbol{w}}(\boldsymbol{s}) \triangleq \omega_\psi(0)\, \boldsymbol{w}\, \mathbf{1}'_N, \tag{H.4}$$

and when $M > N$ (tall case):

$$G^{\mathrm{R}}_{\psi,\boldsymbol{w}}(\boldsymbol{s}) \triangleq \mathbf{1}_M(\boldsymbol{w} \odot \omega_\psi.(\boldsymbol{s}))', \tag{H.5}$$

$$G^{\mathrm{L}}_{\psi,\boldsymbol{w}}(\boldsymbol{s}) \triangleq \omega_\psi(0)\, \mathbf{1}_M\, \boldsymbol{w}'. \tag{H.6}$$

The following theorem states that $Q_{\boldsymbol{w}}(\cdot\,; \boldsymbol{S}, G^{\mathrm{R}}_{\psi,\boldsymbol{w}})$ and $Q_{\boldsymbol{w}}(\cdot\,; \boldsymbol{S}, G^{\mathrm{L}}_{\psi,\boldsymbol{w}})$ are majorizers for $R_{\psi,\boldsymbol{w}}$ at $\boldsymbol{S} \in \mathbb{C}^{M\times N}$, and it also provides equivalent expressions for both functions.

**Theorem H.1** (Majorizers for weighted Huber-based low-rank regularizers).
*Let $\boldsymbol{S} \in \mathbb{C}^{M\times N}$ and $\boldsymbol{U}, \boldsymbol{V}$ denote suitably sized unitary matrices such that $\boldsymbol{S} = \boldsymbol{U}\,\mathsf{Diag}\{\boldsymbol{\sigma}(\boldsymbol{S})\}\,\boldsymbol{V}'$. Let $R_{\psi,\boldsymbol{w}}$ be defined as in (1.8) with nondecreasing weights,* i.e., $0 \leq w_1 \leq w_2 \leq \ldots \leq w_r$. *Then $Q_{\boldsymbol{w}}(\cdot\,; \boldsymbol{S}, G^{\mathrm{R}}_{\psi,\boldsymbol{w}})$ and $Q_{\boldsymbol{w}}(\cdot\,; \boldsymbol{S}, G^{\mathrm{L}}_{\psi,\boldsymbol{w}})$ are both majorizers for $R_{\psi,\boldsymbol{w}}$ at $\boldsymbol{S} \in \mathbb{C}^{M\times N}$,* i.e., *both satisfy (H.1) and (H.2). If $M < N$ (wide case), then*

$$Q_{\boldsymbol{w}}(\boldsymbol{X}; \boldsymbol{S}, G^{\mathrm{R}}_{\psi,\boldsymbol{w}}) = R_{\psi,\boldsymbol{w}}(\boldsymbol{S}) + \mathrm{real}\{\langle \nabla R_{\psi,\boldsymbol{w}}(\boldsymbol{S}),\, \boldsymbol{X} - \boldsymbol{S}\rangle\} + \frac{1}{2}\left\| \boldsymbol{W}'_{\psi,\boldsymbol{S},\boldsymbol{w}}\,(\boldsymbol{X} - \boldsymbol{S})\right\|_{\mathrm{F}}^2, \tag{H.7}$$

$$Q_{\boldsymbol{w}}(\boldsymbol{X}; \boldsymbol{S}, G^{\mathrm{L}}_{\psi,\boldsymbol{w}}) = R_{\psi,\boldsymbol{w}}(\boldsymbol{S}) + \mathrm{real}\{\langle \nabla R_{\psi,\boldsymbol{w}}(\boldsymbol{S}),\, \boldsymbol{X} - \boldsymbol{S}\rangle\} + \frac{1}{2}\,\omega_\psi(0)\left\| \boldsymbol{L}'_{\psi,\boldsymbol{S},\boldsymbol{w}}\,(\boldsymbol{X} - \boldsymbol{S})\right\|_{\mathrm{F}}^2, \tag{H.8}$$

*where the matrices* $\boldsymbol{W}_{\psi,\boldsymbol{S},\boldsymbol{w}}$ *and* $\boldsymbol{L}_{\psi,\boldsymbol{S},\boldsymbol{w}}$ *are defined as:*

$$\boldsymbol{W}_{\psi,\boldsymbol{S},\boldsymbol{w}} \triangleq \boldsymbol{U}\,\mathsf{Diag}\left\{\sqrt{\boldsymbol{w}\odot(\omega_\psi.(\boldsymbol{\sigma}(\boldsymbol{s})))}\right\}\boldsymbol{V}\in\mathbb{C}^{M\times N}. \tag{H.9}$$

$$\boldsymbol{L}_{\psi,\boldsymbol{S},\boldsymbol{w}} \triangleq \boldsymbol{U}\,\mathsf{Diag}\left\{\sqrt{\boldsymbol{w}}\right\}\boldsymbol{V}\in\mathbb{C}^{M\times N}. \tag{H.10}$$

*If* $M>N$ *(tall case), then*

$$Q_{\boldsymbol{w}}(\boldsymbol{X};\boldsymbol{S},G^{\mathrm{R}}_{\psi,\boldsymbol{w}}) = R_{\psi,\boldsymbol{w}}(\boldsymbol{S}) + \mathrm{real}\{\langle\nabla R_{\psi,\boldsymbol{w}}(\boldsymbol{S}),\,\boldsymbol{X}-\boldsymbol{S}\rangle\} + \frac{1}{2}\left\|(\boldsymbol{X}-\boldsymbol{S})\,\boldsymbol{T}'_{\psi,\boldsymbol{S},\boldsymbol{w}}\right\|_{\mathrm{F}}^2, \tag{H.11}$$

$$Q_{\boldsymbol{w}}(\boldsymbol{X};\boldsymbol{S},G^{\mathrm{L}}_{\psi,\boldsymbol{w}}) = R_{\psi,\boldsymbol{w}}(\boldsymbol{S}) + \mathrm{real}\{\langle\nabla R_{\psi,\boldsymbol{w}}(\boldsymbol{S}),\,\boldsymbol{X}-\boldsymbol{S}\rangle\} + \frac{1}{2}\,\omega_\psi(0)\left\|(\boldsymbol{X}-\boldsymbol{S})\,\boldsymbol{H}'_{\psi,\boldsymbol{S},\boldsymbol{w}}\right\|_{\mathrm{F}}^2, \tag{H.12}$$

*where the matrices* $\boldsymbol{T}_{\psi,\boldsymbol{S},\boldsymbol{w}}$ *and* $\boldsymbol{H}_{\psi,\boldsymbol{S},\boldsymbol{w}}$ *are defined as:*

$$\boldsymbol{T}_{\psi,\boldsymbol{S},\boldsymbol{w}} \triangleq \boldsymbol{U}'\,\mathsf{Diag}\left\{\sqrt{\boldsymbol{w}\odot(\omega_\psi.(\boldsymbol{\sigma}(\boldsymbol{s})))}\right\}\boldsymbol{V}'\in\mathbb{C}^{M\times N}. \tag{H.13}$$

$$\boldsymbol{H}_{\psi,\boldsymbol{S},\boldsymbol{w}} \triangleq \boldsymbol{U}'\,\mathsf{Diag}\left\{\sqrt{\boldsymbol{w}}\right\}\boldsymbol{V}'\in\mathbb{C}^{M\times N}. \tag{H.14}$$

The proof for this theorem is not provided as it is analogous to the proof of Theorem 3.1 in Appendix B.

## Appendix I. Proof of proposition 4.6.

Let $\boldsymbol{X},\boldsymbol{S}\in\mathbb{C}^{M\times N}$ and $\boldsymbol{U},\boldsymbol{V}$ denote suitable sized unitary matrices such that $\boldsymbol{S}=\boldsymbol{U}\,\mathsf{Diag}\{\boldsymbol{\sigma}(\boldsymbol{S})\}\,\boldsymbol{V}'$. Without loss of generality we assume that $M<N$ (wide case). By Theorem H.1 we have that:

$$\begin{aligned} R_{\psi,\boldsymbol{w}}(\boldsymbol{X}) &\le Q_{\boldsymbol{w}}(\boldsymbol{X};\boldsymbol{S},G^{\mathrm{L}}_{\psi,\boldsymbol{w}}) \\ &= R_{\psi,\boldsymbol{w}}(\boldsymbol{S}) + \mathrm{real}\{\langle\nabla R_{\psi,\boldsymbol{w}}(\boldsymbol{S}),\,\boldsymbol{X}-\boldsymbol{S}\rangle\} \\ &\quad + \frac{1}{2}\mathbf{1}'_M(G^{\mathrm{L}}_{\psi,\boldsymbol{w}}(\boldsymbol{\sigma}(\boldsymbol{S}))\odot|\boldsymbol{U}'(\boldsymbol{X}-\boldsymbol{S})\boldsymbol{V}|.^\wedge 2)\mathbf{1}_N. \end{aligned} \tag{I.1}$$

We write the last term on the right-hand-side of the previous inequality as follows:

$$\frac{1}{2}\mathbf{1}'_M(G^{\mathrm{L}}_{\psi,\boldsymbol{w}}(\boldsymbol{\sigma}(\boldsymbol{S}))\odot|\boldsymbol{U}'(\boldsymbol{X}-\boldsymbol{S})\boldsymbol{V}|.^\wedge 2)\mathbf{1}_N = \frac{1}{2}\,\omega_\psi(0)\sum_{k=1}^{M} w_k \sum_{l=1}^{N}|[\boldsymbol{U}'(\boldsymbol{X}-\boldsymbol{S})\boldsymbol{V}]_{kl}|^2. \tag{I.2}$$

By replacing this in (I.1) it follows that:

$$\begin{aligned} R_{\psi,\boldsymbol{w}}(\boldsymbol{X}) &\le R_{\psi,\boldsymbol{w}}(\boldsymbol{S}) + \mathrm{real}\{\langle\nabla R_{\psi,\boldsymbol{w}}(\boldsymbol{S}),\,\boldsymbol{X}-\boldsymbol{S}\rangle\} + \frac{1}{2}\,\omega_\psi(0)\sum_{k=1}^{M} w_k \sum_{l=1}^{N}|[\boldsymbol{U}'(\boldsymbol{X}-\boldsymbol{S})\boldsymbol{V}]_{kl}|^2 \\ &\le R_{\psi,\boldsymbol{w}}(\boldsymbol{S}) + \mathrm{real}\{\langle\nabla R_{\psi,\boldsymbol{w}}(\boldsymbol{S}),\,\boldsymbol{X}-\boldsymbol{S}\rangle\} + \frac{1}{2}\,\|\boldsymbol{w}\|_\infty\,\omega_\psi(0)\sum_{k=1}^{M}\sum_{l=1}^{N}|[\boldsymbol{U}'(\boldsymbol{X}-\boldsymbol{S})\boldsymbol{V}]_{kl}|^2 \\ &= R_{\psi,\boldsymbol{w}}(\boldsymbol{S}) + \mathrm{real}\{\langle\nabla R_{\psi,\boldsymbol{w}}(\boldsymbol{S}),\,\boldsymbol{X}-\boldsymbol{S}\rangle\} + \frac{1}{2}\,\|\boldsymbol{w}\|_\infty\,\omega_\psi(0)\left\|\boldsymbol{U}'(\boldsymbol{X}-\boldsymbol{S})\boldsymbol{V}\right\|_{\mathrm{F}}^2 \\ &= R_{\psi,\boldsymbol{w}}(\boldsymbol{S}) + \mathrm{real}\{\langle\nabla R_{\psi,\boldsymbol{w}}(\boldsymbol{S}),\,\boldsymbol{X}-\boldsymbol{S}\rangle\} + \frac{1}{2}\,\|\boldsymbol{w}\|_\infty\,\omega_\psi(0)\,\|\boldsymbol{X}-\boldsymbol{S}\|_{\mathrm{F}}^2, \end{aligned} \tag{I.3}$$

using unitary invariance of the Frobenius norm. Then (I.3) is equivalent to $\nabla R_{\psi,\boldsymbol{w}}$ being $L$-Lipschitz where $L = \|\boldsymbol{w}\|_\infty \omega_\psi(0)$ [2, Thm. 5.8] when considering the inner product in (2.7).

## Appendix J. Pseudocode for the nonlinear conjugate gradient algorithm (NCG).

Algorithm J.1 provides the pseudocode for implementing NCG to solve (1.5) as done in the experiments in Section 6 using the Fletcher-Reeves rule for the conjugate gradient parameter update. We display a convergence criterion based on the gradient norm; however, our experiments did not use this criterion as we wanted to analyze convergence using (6.5).

**Algorithm J.1** Nonlinear conjugate gradient algorithm for solving (1.5)

**Require:** $\boldsymbol{X}_0 \in \mathbb{C}^{M\times N}$ (initial estimation), $\alpha_0$ (initial step size), $n_\alpha \in \mathbb{N}$ (number of iterations for the MM step-size selection strategy), $M_{\text{iter}} \in \mathbb{N}$ (number of iterations), $\eta \in \mathbb{R}$ (convergence threshold)

$\boldsymbol{G}_0 = \nabla \Psi_{\text{Local}}(\boldsymbol{X}_0)$ (initial gradient calculation using (5.1) and (2.9))
$\boldsymbol{\Delta}_0 = -\boldsymbol{G}_0$ (initial search direction)
**for** $k = 0, 1, \ldots, M_{\text{iter}} - 1$ **do**
    $\alpha_k \leftarrow \alpha_0$
    **for** $l = 1, \ldots, n_\alpha$ **do** (MM step-size selection)
        $\alpha_k \leftarrow \alpha_k - \frac{c_h^{(1)}(\alpha_k, \boldsymbol{X}_k, \boldsymbol{\Delta}_k)}{c_h^{(2)}(\alpha_k, \boldsymbol{X}_k, \boldsymbol{\Delta}_k, G_\psi)}$ (using (5.11) and (5.12))
    **end for**
    $\boldsymbol{X}_{k+1} \leftarrow \boldsymbol{X}_k + \alpha_k \boldsymbol{\Delta}_k$ (estimation update)
    $\boldsymbol{G}_{k+1} \leftarrow \nabla \Psi_{\text{Local}}(\boldsymbol{X}_{k+1})$ (gradient calculation using (5.1) and (2.9))
    $\beta_k \leftarrow \|\boldsymbol{G}_{k+1}\|_{\text{F}}^2 / \|\boldsymbol{G}_k\|_{\text{F}}^2$ (conjugate gradient parameter update using Fletcher-Reeves rule)
    $\boldsymbol{\Delta}_{k+1} \leftarrow -\boldsymbol{G}_{k+1} + \beta_k \boldsymbol{\Delta}_k$ (search direction update)
    **if** $\|\boldsymbol{G}_{k+1}\|_{\text{F}} < \eta$ **then**
        **break**
    **end if**
**end for**

## REFERENCES


[1] H. Bauschke, R. Goebel, Y. Lucet, and X. Wang, *The proximal average: basic theory*, SIAM J. Optim., 19 (2008), pp. 766–85, https://doi.org/10.1137/070687542.

[2] A. Beck, *First-order methods in optimization*, Soc. Indust. Appl. Math., 2017, http://bookstore.siam.org/mo25/.

[3] J. Bezanson, A. Edelman, S. Karpinski, and V. B. Shah, *Julia: A fresh approach to numerical computing*, SIAM Review, 59 (2017), pp. 65–98, https://doi.org/10.1137/141000671.

[4] B. Bilgic, T. H. Kim, C. Liao, M. K. Manhard, L. L. Wald, J. P. Haldar, and K. Setsompop, *Improving parallel imaging by jointly reconstructing multi-contrast data*, Magn. Reson. Med., 80 (2018), pp. 619–632.

[5] E. J. Candes, X. Li, Y. Ma, and J. Wright, *Robust principal component analysis?*, J. Assoc. Comput. Mach., 58 (2011), pp. 1–37, https://doi.org/10.1145/1970392.1970395.

[6] J. S. Cavazos, J. A. Fessler, and L. Balzano, *ALPCAH: Subspace learning for sample-wise heteroscedastic data*, IEEE Trans. Signal Process., (2025).

[7] P. Charbonnier, L. Blanc-Feraud, G. Aubert, and M. Barlaud, *Deterministic edge-preserving regularization in computed imaging*, IEEE Trans. Im. Proc., 6 (1997), pp. 298–311, https://doi.org/10.1109/83.551699.

[8] K. Chen, H. Dong, and K.-S. Chan, *Reduced rank regression via adaptive nuclear norm penalization*, Biometrika, 100 (2013), pp. 901–920.

[9] X. Chen et al., *Improved structured low-rank reconstruction for 3D multi-shot EPI with joint motion modelling*, in ISMRM Workshop on Data Sampling and Image Reconstruction, 2023.

[10] Y. Chen and Y. Chi, *Harnessing structures in big data via guaranteed low-rank matrix estimation: Recent theory and fast algorithms via convex and nonconvex optimization*, IEEE Sig. Proc. Mag., 35 (2018), pp. 14–31, https://doi.org/10.1109/msp.2018.2821706.

[11] Y. Chi, *Low-rank matrix completion*, IEEE Sig. Proc. Mag., 35 (2018), pp. 178–81, https://doi.org/10.1109/msp.2018.2832197.

[12] Y. Chi, Y. M. Lu, and Y. Chen, *Nonconvex optimization meets low-rank matrix factorization: an overview*, IEEE Trans. Sig. Proc., 67 (2019), pp. 5239–69, https://doi.org/10.1109/tsp.2019.2937282.

[13] A. G. Christodoulou and S. G. Lingala, *Accelerated dynamic magnetic resonance imaging using learned representations: a new frontier in biomedical imaging*, IEEE Signal Process. Mag., 37 (2020), pp. 83–93.

[14] C. K. Chu, I. K. Glad, F. Godtliebsen, and J. S. Marron, *Edge-preserving smoothers for image processing*, J. Am. Stat. Assoc., 93 (1998), pp. 526–56.

[15] P.-A. Comby, Z. Amor, A. Vignaud, and P. Ciuciu, *Denoising of fMRI volumes using local low rank methods*, 2023, https://hal.science/hal-03895194.

[16] G. Cruz, A. Hua, C. Munoz, T. F. Ismail, A. Chiribiri, R. M. Botnar, and C. Prieto, *Low-rank motion correction for accelerated free-breathing first-pass myocardial perfusion imaging*, Magn. Reson. Med., 90 (2023), pp. 64–78.

[17] S. Das Gupta, R. M. Freund, X. A. Sun, and A. Taylor, *Nonlinear conjugate gradient methods: worst-case convergence rates via computer-assisted analyses*, Math. Program., (2024), pp. 1–49.

[18] M. A. Davenport and J. Romberg, *An overview of low-rank matrix recovery from incomplete observations*, IEEE J. Sel. Top. Sig. Proc., 10 (2016), pp. 608–22, https://doi.org/10.1109/jstsp.2016.2539100.

[19] J. A. Fessler and S. D. Booth, *Conjugate-gradient preconditioning methods for shift-variant PET image reconstruction*, IEEE Trans. Im. Proc., 8 (1999), pp. 688–99, https://doi.org/10.1109/83.760336.

[20] S. Guo, J. A. Fessler, and D. C. Noll, *High-resolution oscillating steady-state fMRI using patch-tensor low-rank reconstruction*, IEEE Trans. Med. Imag., 39 (2020), pp. 4357–68, https://doi.org/10.1109/TMI.2020.3017450.

[21] W. W. Hager and H. Zhang, *A survey of nonlinear conjugate gradient methods*, Pacific J. Optim., 2 (2006), pp. 35–58.

[22] J. P. Haldar, *Low-rank modeling of local k-space neighborhoods (LORAKS) for constrained MRI*, IEEE Trans. Med. Imag., 33 (2014), pp. 668–81, https://doi.org/10.1109/TMI.2013.2293974.

[23] J. P. Haldar and K. Setsompop, *Linear predictability in MRI reconstruction: Leveraging shift-invariant Fourier structure for faster and better imaging*, IEEE Sig. Proc. Mag., 37 (2020), pp. 69–82,

https://doi.org/10.1109/MSP.2019.2949570.
[24] J. P. Haldar and J. Zhuo, *P-LORAKS: low-rank modeling of local k-space neighborhoods with parallel imaging data*, Magn. Reson. Med., 75 (2016), pp. 1499–1514.
[25] R. A. Horn and C. R. Johnson, *Matrix analysis*, Cambridge University Press, 2012.
[26] P. J. Huber, *Robust statistics*, Wiley, New York, 1981.
[27] M. Jacob, M. P. Mani, and J. C. Ye, *Structured low-rank algorithms: theory, MR applications, and links to machine learning*, IEEE Sig. Proc. Mag., 37 (2020), pp. 54–68, https://doi.org/10.1109/MSP.2019.2950432.
[28] K. H. Jin, D. Lee, and J. C. Ye, *A general framework for compressed sensing and parallel MRI using annihilating filter based low-rank Hankel matrix*, IEEE Trans. Computational Imaging, 2 (2016), pp. 480–95, https://doi.org/10.1109/tci.2016.2601296.
[29] R. A. Jones, O. Haraldseth, T. B. Mueller, P. A. Rinck, and A. N. Oksendal, *K-space substitution: A novel dynamic imaging technique*, Mag. Res. Med., 29 (1993), pp. 830–4, https://doi.org/10.1002/mrm.1910290618.
[30] Z. Ke, W. Huang, Z.-X. Cui, J. Cheng, S. Jia, H. Wang, X. Liu, H. Zheng, L. Ying, Y. Zhu, and D. Liang, *Learned low-rank priors in dynamic MR imaging*, IEEE Trans. Med. Imag., 40 (2021), pp. 3698–710, https://doi.org/10.1109/TMI.2021.3096218.
[31] D. Kim and J. A. Fessler, *Adaptive restart of the optimized gradient method for convex optimization*, J. Optim. Theory Appl., 178 (2018), pp. 240–63, https://doi.org/10.1007/s10957-018-1287-4.
[32] T. H. Kim, K. Setsompop, and J. P. Haldar, *LORAKS makes better SENSE: phase-constrained partial fourier SENSE reconstruction without phase calibration*, Magn. Reson. Med., 77 (2017), pp. 1021–1035.
[33] J. Lee, S. Kim, G. Lebanon, and Y. Singer, *Local low-rank matrix approximation*, in Proc. Intl. Conf. Mach. Learn, vol. 28, 2013, pp. 82–90, https://proceedings.mlr.press/v28/lee13.html.
[34] A. S. Lewis, *The convex analysis of unitarily invariant matrix functions*, Journal of Convex Analysis, 2 (1995), pp. 173–183.
[35] A. S. Lewis, *The convex analysis of unitarily invariant matrix functions*, J. Convex Analysis, 2 (1995), pp. 173–83, https://www.heldermann.de/JCA/jca02.htm.
[36] A. S. Lewis, *Convex analysis on the hermitian matrices*, SIAM Journal on Optimization, 6 (1996), pp. 164–177.
[37] A. S. Lewis and H. S. Sendov, *Twice differentiable spectral functions*, SIAM J. Matrix Anal. Appl., 23 (2001), pp. 368–386.
[38] A. S. Lewis and H. S. Sendov, *Quadratic expansions of spectral functions*, Linear algebra and its applications, 340 (2002), pp. 97–121.
[39] A. S. Lewis and H. S. Sendov, *Nonsmooth analysis of singular values. Part I: Theory*, Set-Valued Analysis, 13 (2005), pp. 213–241.
[40] A. S. Lewis and H. S. Sendov, *Nonsmooth analysis of singular values. Part II: Applications*, Set-Valued Analysis, 13 (2005), pp. 243–264.
[41] Z.-P. Liang and P. C. Lauterbur, *Principles of Magnetic Resonance Imaging: A Signal Processing Perspective*, IEEE Press, 2000.
[42] C. Y. Lin and J. A. Fessler, *Efficient dynamic parallel MRI reconstruction for the low-rank plus sparse model*, IEEE Trans. Computational Imaging, 5 (2019), pp. 17–26, https://doi.org/10.1109/TCI.2018.2882089.
[43] R. A. Lobos, M. U. Ghani, W. C. Karl, R. M. Leahy, and J. P. Haldar, *Autoregression and structured low-rank modeling of sinogram neighborhoods*, IEEE Trans. Computational Imaging, 7 (2021), pp. 1044–54, https://doi.org/10.1109/TCI.2021.3114994.
[44] R. A. Lobos and J. P. Haldar, *On the shape of convolution kernels in MRI reconstruction: Rectangles versus ellipsoids*, Magn. Reson. Med., 87 (2022), pp. 2989–2996.
[45] R. A. Lobos, T. H. Kim, W. S. Hoge, and J. P. Haldar, *Navigator-free EPI ghost correction with structured low-rank matrix models: New theory and methods*, IEEE Trans. Med. Imag., 37 (2018), pp. 2390–2402.
[46] J. Lu, C. Xu, Z. Hu, X. Liu, Q. Jiang, D. Meng, and Z. Lin, *A new nonlocal low-rank regularization method with applications to magnetic resonance image denoising*, Inverse Prob., 38 (2022), p. 065012, https://doi.org/10.1088/1361-6420/ac65ac.

[47] N. K. Meyer, D. Kang, D. F. Black, N. G. Campeau, K. M. Welker, E. M. Gray, M.-H. In, Y. Shu, J. Huston, M. A. Bernstein, and J. D. Trzasko, *Enhanced clinical task-based fMRI metrics through locally low-rank denoising of complex-valued data*, The Neuroradiology J., (2022), p. 19714009221122171, https://doi.org/10.1177/19714009221122171.

[48] L. Mirsky, *Symmetric gauge functions and unitarily invariant norms*, The quarterly journal of mathematics, 11 (1960), pp. 50–9, https://doi.org/10.1093/qmath/11.1.50.

[49] T.-H. Oh, Y.-W. Tai, J.-C. Bazin, H. Kim, and I. S. Kweon, *Partial sum minimization of singular values in robust PCA: Algorithm and applications*, IEEE Trans. Patt. Anal. Mach. Int., 38 (2016), pp. 744–758.

[50] G. Ongie and M. Jacob, *A fast algorithm for convolutional structured low-rank matrix recovery*, IEEE Trans. Computational Imaging, 3 (2017), pp. 535–50, https://doi.org/10.1109/tci.2017.2721819.

[51] R. Otazo, E. Candes, and D. K. Sodickson, *Low-rank plus sparse matrix decomposition for accelerated dynamic MRI with separation of background and dynamic components*, Mag. Res. Med., 73 (2015), pp. 1125–36, https://doi.org/10.1002/mrm.25240.

[52] K. P. Pruessmann, M. Weiger, M. B. Scheidegger, and P. Boesiger, *SENSE: sensitivity encoding for fast MRI*, Magn. Reson. Med., 42 (1999), pp. 952–962.

[53] H. Qi and X. Yang, *Semismoothness of spectral functions*, SIAM J. Matrix Anal. Appl., 25 (2003), pp. 766–783.

[54] M. K. Riahi and I. A. Qattan, *On the convergence rate of Fletcher-Reeves nonlinear conjugate gradient methods satisfying strong Wolfe conditions: Application to parameter identification in problems governed by general dynamics*, Math. Meth. Appl. Sci., 45 (2022), pp. 3644–64, https://doi.org/https://doi.org/10.1002/mma.8009.

[55] R. T. Rockafellar, *Convex analysis*, Princeton University Press, Princeton, 1970.

[56] A. Saucedo, S. Lefkimmiatis, N. Rangwala, and K. Sung, *Improved computational efficiency of locally low rank MRI reconstruction using iterative random patch adjustments*, IEEE Trans. Med. Imag., 36 (2017), pp. 1209–1220.

[57] H. S. Sendov, *Generalized Hadamard product and the derivatives of spectral functions*, SIAM J. Matrix Anal. Appl., 28 (2006), pp. 667–681.

[58] H. S. Sendov, *The higher-order derivatives of spectral functions*, Linear Algebra Appl., 424 (2007), pp. 240–281.

[59] J. I. Tamir, M. Uecker, W. Chen, P. Lai, M. T. Alley, S. S. Vasanawala, and M. Lustig, *T2 shuffling: sharp, multicontrast, volumetric fast spin-echo imaging*, Mag. Res. Med., 77 (2017), pp. 180–95, https://doi.org/10.1002/mrm.26102.

[60] A. B. Taylor, J. M. Hendrickx, and F. Glineur, *Exact worst-case performance of first-order methods for composite convex optimization*, SIAM J. Optim., 27 (2017), pp. 1283–313, https://doi.org/10.1137/16m108104x.

[61] J. Trzasko, *Stochastic primal-dual optimization for locally low-rank MRI reconstruction: A stable alternative to cycle spinning*, in Proc. Intl. Soc. Mag. Res. Med., 2017, p. 0455, http://archive.ismrm.org/2017/0455.html.

[62] J. Trzasko and A. Manduca, *Local versus global low-rank promotion in dynamic MRI series reconstruction*, in Proc. Intl. Soc. Mag. Res. Med., 2011, p. 4371, http://dev.ismrm.org//2011/4371.html.

[63] J. D. Trzasko and A. Manduca, *Calibrationless parallel MRI using CLEAR*, in 2011 conference record of the forty fifth Asilomar conference on signals, systems and computers (ASILOMAR), IEEE, 2011, pp. 75–79.

[64] M. Udell, C. Horn, R. Zadeh, and S. Boyd, *Generalized low rank models*, Found. & Trends in Machine Learning, 9 (2016), pp. 1–118, https://doi.org/10.1561/2200000055.

[65] L. Vizioli, S. Moeller, L. Dowdle, M. Akcakaya, F. D. Martino, E. Yacoub, and K. Ugurbil, *Lowering the thermal noise barrier in functional brain mapping with magnetic resonance imaging*, Nature Comm., 12 (2021), p. 5181, https://doi.org/10.1038/s41467-021-25431-8.

[66] F. Wen, L. Chu, P. Liu, and R. C. Qiu, *A survey on nonconvex regularization-based sparse and low-rank recovery in signal processing, statistics, and machine learning*, IEEE Access, 6 (2018), pp. 69883–906, https://doi.org/10.1109/ACCESS.2018.2880454.

[67] B. Yaman, S. Weingartner, N. Kargas, N. D. Sidiropoulos, and M. Akcakaya, *Locally low-rank tensor regularization for high-resolution quantitative dynamic MRI*, in Proc. Intl. Wkshp. Comp. Adv.

Multi-Sensor Adapt. Proc., 2017, https://doi.org/10.1109/CAMSAP.2017.8313075.

[68] Y. Yang, Y. Feng, and J. A. K. Suykens, *Robust low-rank tensor recovery with regularized redescending M-estimator*, IEEE Trans. Neural Net. Learn. Sys., 27 (2016), pp. 1933–46, https://doi.org/10.1109/TNNLS.2015.2465178.

[69] Z. Zha, B. Wen, X. Yuan, S. Ravishankar, J. Zhou, and C. Zhu, *Learning nonlocal sparse and low-rank models for image compressive sensing: nonlocal sparse and low-rank modeling*, IEEE Sig. Proc. Mag., 40 (2023), pp. 32–44, https://doi.org/10.1109/MSP.2022.3217936.

[70] T. Zhang, J. M. Pauly, and I. R. Levesque, *Accelerating parameter mapping with a locally low rank constraint*, Mag. Res. Med., 73 (2015), pp. 655–61, https://doi.org/10.1002/mrm.25161.

[71] X. Zhang, D. Guo, Y. Huang, Y. Chen, L. Wang, F. Huang, Q. Xu, and X. Qu, *Image reconstruction with low-rankness and self-consistency of k-space data in parallel MRI*, Med. Im. Anal., 63 (2020), p. 101687, https://doi.org/10.1016/j.media.2020.101687.

[72] X. Zhang, H. Lu, D. Guo, Z. Lai, H. Ye, X. Peng, B. Zhao, and X. Qu, *Accelerated MRI reconstruction with separable and enhanced low-rank Hankel regularization*, IEEE Trans. Med. Imag., 41 (2022), pp. 2486–98, https://doi.org/10.1109/TMI.2022.3164472.